Coordination Chemistry Reviews 254 (2010) 890–915

Contents lists available at ScienceDirect

Coordination Chemistry Reviews

journal homepage: www.elsevier.com/locate/ccr

Review

Coordination complexes incorporating pyrophosphate: Structural overview and exploration of their diverse magnetic, catalytic and biological properties

Oluwatayo F. Ikotun[a], Nadia Marino[a,*], Paul E. Kruger[b], Miguel Julve[c], Robert P. Doyle[a,*]

[a] Department of Chemistry, Syracuse University, Syracuse, NY 13244-4100, USA
[b] Department of Chemistry, College of Science, University of Canterbury, Christchurch, 8020, New Zealand
[c] Department of Química Inorgànica/Instituto de Ciencia Molecular, Universitat de València, Polígono La Coma s/n, E-46980 Paterna, València, Spain

Contents

Abbreviations: PPi, inorganic pyrophosphate (diphosphate); NTP, nucleoside triphosphate; PPases, pyrophosphatases; VPO, vanadium-phosphorus(V)-oxide catalyst; VHP, vanadyl hydrogen-phosphate hemihydrate; VPP, vanadyl pyrophosphate; RT, room temperature; $Htmp^+$, 2,4,6-trimethylpidinium; $Hdma\text{-}dmn^+$, 1-dimethylammonio-8-dimethylaminonaphthalene; tren, tris(2-aminoethyl)amine; $Hdma^+$, 2,3-dimethylanilinium; $Hetma^+$, 2-ethyl-6-methylanilinium; H_2dap^{2+}, 1,3-diammoniumpropane; en, ethylenediamine; H_2en^{2+}, ethylenediammonium; phen, 1,10-phenanthroline; bipy, 2,2′-bipyridine; bpym, 2,2′-bipyrimidine; tpa, tris(2-pyridylmethyl)amine; chd, *trans*-1,2-cyclohexanediamine; dpa, di(2-pyridyl)amine; NPY, N-biphenyl-N-pyridine; NBu_4^+, tetrabutylammonium cation; NMe_3Ph^+, trimethylphenylammonium cation; CH_3COO^-, acetate anion; $HCOO^-$, formate anion; py, pyridine.

* Corresponding author. Fax: +1 315 443 4070.
E-mail addresses: nmarino@syr.edu (N. Marino), rpdoyle@syr.edu (R.P. Doyle).

0010-8545/$ – see front matter
doi:10.1016/j.ccr.2009.12.015

ARTICLE INFO

Article history:
Received 19 September 2009
Accepted 8 December 2009
Available online 14 December 2009

Keywords:
Pyrophosphate
X-ray crystal structures
Magnetism
Cytotoxicity
Diphosphate

ABSTRACT

Current attention continues to revolve around the chemistry and biochemistry associated with polyphosphate anions because of their importance in biology. A pivotal intermediate within this family is the pyrophosphate tetraanion, $P_2O_7^{4-}$. Considering its biological relevance and the multidentate nature that makes it an ideal ligand in the field of the coordination chemistry, there is a growing interest in the use of this anion in building new class of molecules/compounds for different purposes. While the total number of characterized structures still remains modest, several new pyrophosphate-containing coordination complexes have been reported in the last decade, as well as different solid-state structures. This review focuses on the structural, magnetic, and biological properties of coordination complexes incorporating the pyrophosphate ligand reported to date.

1. Introduction

Inorganic pyrophosphate (PPi) is a diphosphate tetraanion ($[O_3P\text{-}O\text{-}PO_3]^{4-}$) that is ubiquitous in nature [1,2] PPi plays a central role in a variety of bioenergetic processes [3,4] the –P–O–P– moiety acting, for instance, as the main chemical form in which energy is circulated in living cells [5,6]. Pyrophosphate has also been shown to be pivotal in certain catalytic processes such as the conversion of butane to maleic anhydride [7–9]. More recently, significant efforts have been devoted to check its ability in mediating magnetic interactions between paramagnetic transition metal ions [10–16] and to investigate its potentiality and effectiveness as a component of drugs/prodrugs [17,18]. This review will tie together early seminal work with rapid recent developments, focusing on the coordination chemistry of pyrophosphate and the properties of the compounds that incorporate the anion as a ligand.

1.1. Biological significance of pyrophosphate

PPi is produced during a variety of biosynthetic reactions, including the biosynthesis of nucleotides, lipids, urea, oxidative phosphorylation [1] and other NTP-dependent reactions [3,19]. PPi is also a common reactant in major metabolic pathways including fat metabolism, protein synthesis, nucleoside diphosphate sugar synthesis, DNA and RNA synthesis (see Fig. 1) [20]. The free $P_2O_7^{4-}$ anion is unstable in aqueous solutions and rapidly hydrolyzes to inorganic phosphate in the presence of divalent metal ions ($P_2O_7^{4-} + H_2O \rightarrow 2HPO_4^{2-}$), which enhance cleavage of both inorganic and biological pyrophosphates, especially in acidic conditions [21,22].

1.1.1. Enzymatic function

Biological pyrophosphates are hydrolyzed by a family of enzymes known as pyrophosphatases (PPases) [23]. PPases are classified into soluble or membrane-bound [24,25]. Soluble pyrophosphatases (sPPases) are ubiquitous, found in all organisms, in two forms: (i) organic and (ii) inorganic [26] (i) Organic PPases hydrolyze pyrophosphoric bonds coupled to organic residues, while the inorganic PPases hydrolyze free pyrophosphate. These enzymes are essential for the regulation of intra-cellular levels of inorganic phosphate and for the removal of pyrophosphate products of nucleotide coupling reactions [23,27]. (ii) There are two unrelated families of inorganic pyrophosphatases, the ubiquitous Mg-dependent Family I and the Mn-dependent Family II found in bacteria and archaea [97]. The soluble pyrophosphatases have several roles including some steroid biosynthetic pathways (such as juvenile hormone synthesis), regulation of cell motility, nucleotide metabolism, and may have a nuclear role in regulating transcription of some genes [26,28,29]. Like many enzymes having ATP or other nucleoside triphosphates, PPases require divalent metal cations for activity. The efficiency of such cations as activator decreases in the order: Mg(II) > Zn(II) > Co(II) > Mn(II) > Cd(II) [30,31]. These enzymes can have as many as four functional divalent metal ions in the active site, with two metal ions bound as essential cofactors, whereas the third and fourth are ligated to pyrophosphate/phosphate forming motifs [30,31]. The membrane-bound inorganic pyrophosphatases work as proton pumps, coupling pyrophosphate hydrolysis with electrogenic translocation of protons [23,27,32]. The proton-pyrophosphatases (H^+-PPases) have been found in plant vacuoles, chromatophore of photosynthetic bacteria, archeobacteria, plasma membranes and acidocalcisomes of parasites [33–35].

Of note also is the requirement for some Family I pyrophosphatases for 'unusual' metal cofactors such as the Ca-dependent mitochondrial pyrophosphatase of Leishmania major [98] and the Zn- and Fe-dependent enzymes of some anoxygenic photosynthetic bacteria [99].

Finally, pyrophosphate has also been shown to increase the efficiency of enterobactin-dependent iron uptake in *Escherichia coli* [100]. This work demonstrates that pyrophosphate acts as an iron-chelating agent, trigger the siderophore-dependent iron uptake system and promotes an increased binding of iron to the siderophore.

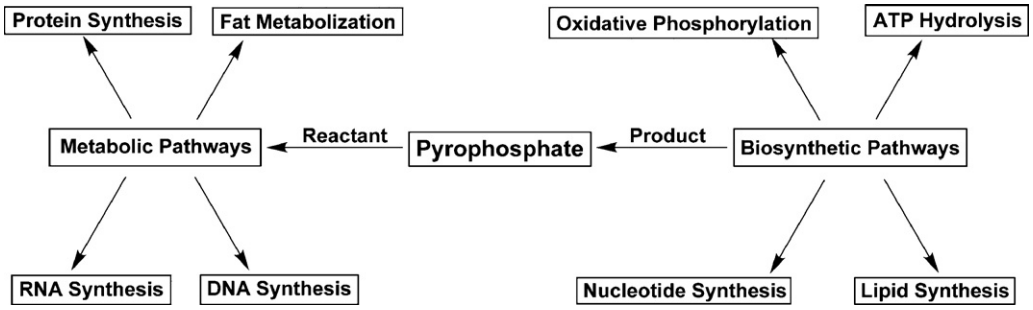

Fig. 1. Bio-energetic processes in which pyrophosphate either functions as a reactant or is formed as a product.

1.2. Catalytic significance of vanadium pyrophosphate

The vanadium-phosphorus(V)-oxide (VPO) catalyst is the only commercial catalyst for selective oxidation of butane to maleic anhydride [8,36]. The process achieves approximately 80% selectivity and 50% conversion, while performing a 14-electron oxidation that involves the abstraction of eight hydrogen atoms and the insertion of three oxygen atoms [7,37].

This selective oxidation was first described in 1966 by Bergman and Frisch [38]. Since commercialization in 1974, this route has replaced the use of benzene in over 70% of maleic anhydride production worldwide [9].

Over the past four decades, the VPO system has been extensively studied, inspired by the necessity to clarify the nature of both the precursor species [39–41] and the active phase of the catalyst [36,42–46], as well as to investigate the oxidation reaction mechanism [7–9].

The active and selective phase for this reaction has been identified as vanadyl pyrophosphate (VPP), $(VO)_2P_2O_7$ [8]. Although this seems to be now well established, the complexity of the solid-state chemistry of the VPO system has led to some confusion and contradictions in the literature over the years [7]. The most widely used precursor of VPP, at either the academic-research or the commercial–industrial level, is the hemihydrate form of vanadyl hydrogen-phosphate (VHP), $(VO)HPO_4{\cdot}0.5H_2O$ [7,47]. The VHP precursor dehydrates to VPP by terminal treatment at ca. 673 K, undergoing a so-called *topotactic* transformation which has been subject of several studies and object of scientific debates [39,48–51] even after the elucidation of the structure of both phases.

The crystal structure of $(VO)HPO_4{\cdot}0.5H_2O$ was first reported in 1984 by Torardi and Calabrese, at either room (RT) or low temperature (~143 K) [39]. Parallel [40] and following studies [41–43] confirmed the accuracy of the determined unit cell and structural parameters, without adding any improvement to the crystal resolution.

The structural characterization of the actual VPP active catalyst has proved to be a significant challenge, presumably due to difficulties in attaining an unique and perfectly ordered phase at low, catalytically relevant temperatures (~700 K) [46]. In this regard, higher calcination temperatures (close or even above 1000 K) have proven to provide VPP crystals of higher quality [48].

Initial diffraction (X-ray or electron) experiments suggested $(VO)_2P_2O_7$ crystallizing with orthorhombic symmetry (space group *Pcam* or $Pca2_1$) [36,43] then, also the monoclinic $P2_1$ option has been proposed [44]. However, such "crystallographic" ambiguity did not preclude the understanding of the vanadyl units and pyrophosphate groups connectivity in the structure, essential for the formulation of any VHP → VPP conversion mechanism [39,48–50].

Greater insight into the structure of vanadyl pyrophosphate has recently come from attempts to clarify the nature of the intriguing magnetic properties of the system [45,46], which has investigated as a possible realization of the theoretical *spin-ladder* model [52–54]. Hiroi et al. [45] and Geupel et al. [46] have used this to unambiguously established the orthorhombic $Pca2_1$ as the correct space group for the ambient-pressure phase obtained at high temperature (973–1123 K). Different models for the precursor conversion have been proposed so far. At present, the most widely accepted mechanism of transformation is the so-called *phosphorus inversion* mechanism of Torardi and Calabrese [39]. This method has been hypothesized on the basis of a strong structural relationship existing between the two involved species [39,50].

As shown in Fig. 2, the structural unit of VHP is a bis-μ-(HPO_4), mono-μ-H_2O bridged *cis*-vanadyl dimer, with a V···V separation of ~3.1 Å [39–42]. The vanadium ion has a distorted octahedral environment, with the axial positions occupied by an oxygen atom

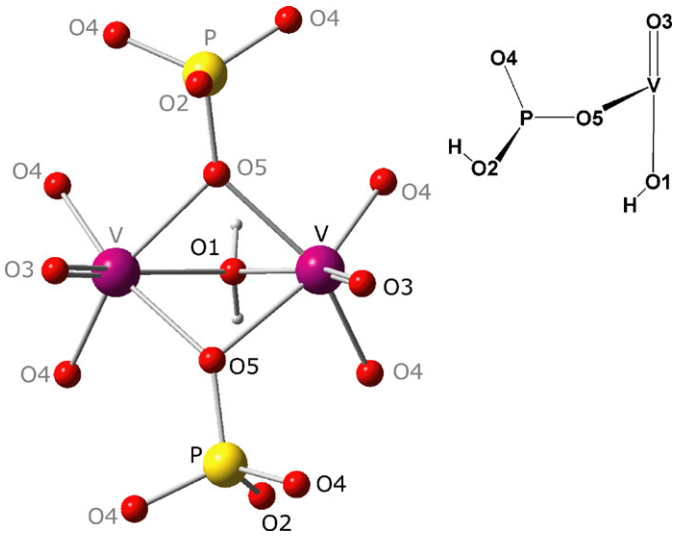

Fig. 2. The structural unit of $VO(HPO_4){\cdot}0.5H_2O$, with the labelling scheme adopted by Torardi and Calabrese [39] (asymmetric unit schematized on the right).

building the vanadyl unit and another one from the coordinated water molecule (with V=O and V–O_w bond distances of ~1.59 and 2.34 Å, respectively), while the equatorial positions are filled by two pairs of symmetry-related oxygen atoms from four different phosphate groups. This connectivity leads to the formation of layers parallel to the crystallographic *ab* plane, held together along the *c*-axis *via* interlayer hydrogen bonding.

In the structure of VPP, the vanadium ions again are hexacoordinated, and their coordination environment is very similar to that found in the VHP precursor. The asymmetric unit consists of two crystallographically independent bis-(P_2O_7) bridged *trans*-vanadyl dimers (V=O bond distance and V···V separation in the range 1.59–1.61 and 3.20–3.23 Å, respectively) and two unique pyrophosphate groups, whose oxygen atoms fill the equatorial positions of the metal distorted octahedral environment [45,46]. The transformation of two hydrogen-phosphate groups into a (fused) pyrophosphate group keeps the phosphate denticity intact (see Scheme 1). The remaining axial position of each vanadyl cation is occupied by an oxygen atom from a symmetry-related vanadyl unit, with long V–O distances ranging from 2.25 to 2.34 Å (note that the V–O_w distance in VHP is ~2.34 Å).

Obviously the site of catalysis lies at the vanadium but pyrophosphate is clearly playing a key role in facilitating the catalysis. The significance of pyrophosphate for the catalytic behavior probably lies in the specific coordination mode it adopts. There has also been much discussion on the importance of the specific nucleophilicity of oxygen from pyrophosphate groups. In addition to structural effects then (probably including site isolation), the particular redox behavior of vanadium(IV), and/or vanadium(V), is being modified by pyrophosphate, with the overall effect being profound on catalytic activity.

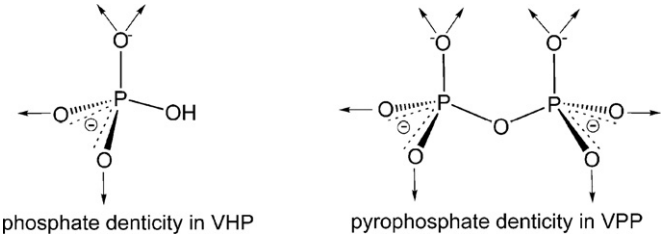

Scheme 1. The fusion of two phosphates into a pyrophosphate group when forming VPP from VHP keeps the phosphate coordination environment intact.

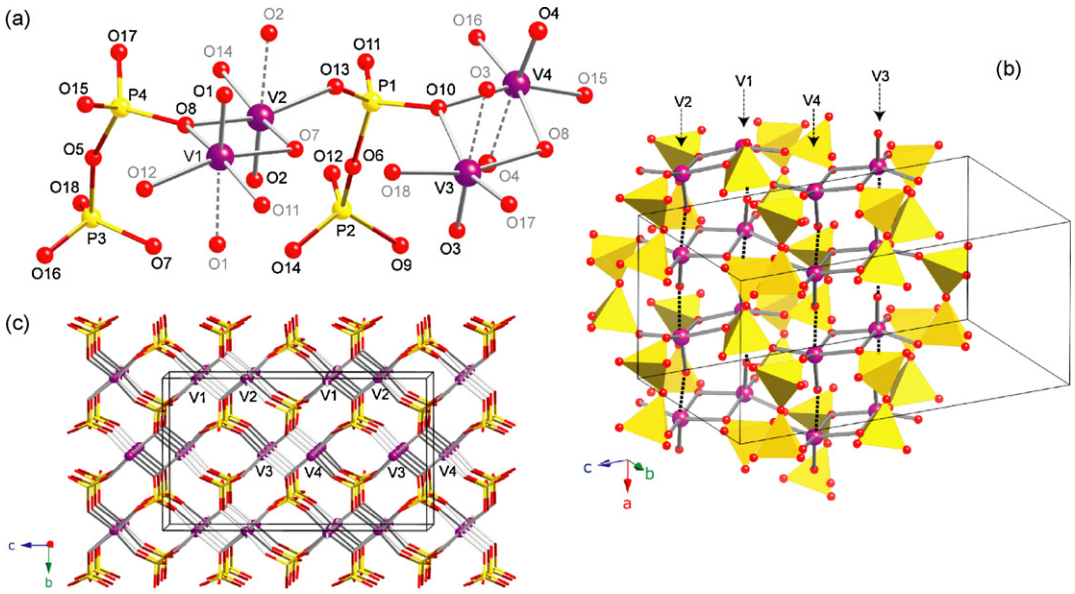

Fig. 3. Structure of the ambient-pressure phase of $(VO)_2P_2O_7$, determined at 120 K from synchrotron X-ray diffraction data [46]: (a) asymmetric unit with the original labelling scheme (the full coordination sphere of the four independent vanadyl ions has been shown for clarity); (b) a view of the two different ladders of vanadyl cations growing along the *a*-axis, emphasizing the V=O···V=O interactions; the polyhedral model has been used for the interconnecting $P_2O_7^{4-}$ groups for clarity; (c) view of the 3D structure in the *bc* plane.

Different crystallographic orientations of the orthorhombic VPP unit cell can be found in the literature. Following the convention of Geupel et al. [46] such infinite axial–V=O–V=O–interaction results in the arrangement of the two crystallographically not-equivalent vanadyl dimers into two corresponding ladder-like chains growing along the *a*-axis (see Fig. 3b). As shown in Fig. 3c, the pyrophosphate bridges connect these chains in either the *b* and *c* direction, contributing to build an overall three-dimensional network (*vs.* the phosphate-directed 2D motif in VHP).

The *anti* arrangement of the vanadyl units found in the crystal structure of VPP (*syn* in the VHP precursor) is believed to play an important role in the oxidation of *n*-butane to maleic anhydride [39]. It must be noted here that the structure of the actual catalyst remains elusive, due in part to the high degree of phase disorder retained at temperatures close to that of the VHP → VPP conversion (∼700 K). This lack of a complete structure means there are still several questions open about the nature and mechanism of *n*-butane activation on the catalyst surface [39].

The difficulty in attaining the crystal structure of the active VPP catalyst has encouraged different attempts to synthesize other vanadyl pyrophosphate-based materials.

In 1997 Herron et al. (*DuPont company*) succeeded in the isolation of an unique vanadyl pyrophosphate species with a discrete tetranuclear core, the compound of formula $A_4[(VO)_4(\mu\text{-}P_2O_7)_2(\mu\text{-}OCH_3)_4]^{4-}$, where A^+ is either the 2,4,6-trimethylpidinium or the 1-dimethylammonio-8-dimethylaminonaphthalene cation (see Section 2.3.1) [55]. The authors investigated the properties of the Hdma-dmn$^+$-based (more soluble) compound by impregnation onto porous silica from concentrated organic solution, followed by drying and calcination under conditions designed to produce the VPO catalyst. The cluster showed moderate catalytic activity, with a selectivity of 30% for butane and conversion of 6% to maleic anhydride. Although those numbers are not comparable to the VPO ones (∼80% selectivity and 50% conversion), the importance of this work resides in providing a new route to approach this important catalytic process, expanding the field toward the coordination chemistry.

At present no vanadyl-pyrophosphate coordination compounds have been tested directly, i.e. without previous conversion into the usual VPP phase. Given the vast commercial application of the VPO catalyst, this further step would be of great interest considering that such complexes may enhance our knowledge regarding the structural properties necessary for the catalytic conversion. For further reading on this topic (with special regards to the reaction mechanism) the authors recommend Centi et al. [7], Chen and Munson [8] and Ballarini et al. [9].

2. Crystal structures of pyrophosphate coordination complexes

Structures of metallo-polyphosphates were first investigated in the 1970s to explore the role of metal ions in the hydrolytic cleavage of phosphates by enzymes (such as ATPases, kinases, and pyrophosphatases) [56,57]. Initially, most studies focused on metal complexation to ATP [58,59] but in order to obtain greater insight into the bonding and reactivity patterns of enzymes that act on oligophosphates, it became important to study the coordination chemistry of pyrophosphate itself [56]. The expansion in that direction began in 1981, with the synthesis of a series of monomeric Cr(III)–pyrophosphate complexes by Sundaralingam and co-workers [60–63]. Since then, pyrophosphate has been demonstrated to be an excellent "non-bridging" ligand for metal ions, mostly due to a certain level of protonation on the effective ligand species ($HP_2O_7^{3-}$ or $H_2P_2O_7^{2-}$), depending upon reaction conditions.

The first metal complex incorporating the (bridging) tetraanionic $P_2O_7^{4-}$ species was accomplished by Ainscough et al. in 1992 [14]. The same authors showed for the first time the ability of the pyrophosphate ligand to mediate magnetic interactions between paramagnetic centres. Despite this, in-depth magneto-structural investigations have only been reported recently (see Section 3) [12].

The number of characterized structures after more than 30 years of research also remains modest. To the best of our knowledge, only 33 metallo-pyrophosphate coordination complexes have been reported to date. This number is reduced to 18 when considering only those complexes that incorporate pyrophosphate as a bridging group (Table 1).

Table 1
Structurally characterized coordination complexes featuring the pyrophosphate ligand ($H_2P_2O_7^{2-}$, $HP_2O_7^{3-}$ or $P_2O_7^{4-}$). Comprehensive crystallographic data can be found in Supplementary Material.

Compound	Metal ion	Ligands	Molecular formula	References	CCD code
Monomers					
1	Cr(III)	$HP_2O_7^{3-}$, NH_3	$[Cr(HP_2O_7)(NH_3)_4]\cdot 2H_2O$	[60]	–
2	Cr(III)	$HP_2O_7^{3-}$, H_2O, NH_3	*mer*-$[Cr(HP_2O_7)(NH_3)_3(H_2O)]\cdot 2H_2O$	[61]	–
3	Cr(III)	$HP_2O_7^{3-}$, H_2O, NH_3	$[Cr(HP_2O_7)(NH_3)_2(H_2O)_2]\cdot H_2O$	[62]	–
4	Cr(III)	$HP_2O_7^{3-}$, H_2O, NH_3	$[Cr(HP_2O_7)(NH_3)_2(H_2O)_2]\cdot 2H_2O$	[62]	–
5	Cr(III)	$HP_2O_7^{3-}$, H_2O	$[Cr(HP_2O_7)(H_2O)_4]\cdot 3H_2O$	[63]	–
6	Co(III)	$H_2P_2O_7^{2-}$, tren	$[Co(H_2P_2O_7)(tren)]ClO_4\cdot H_2O$	[71]	VAXYUO
7	Co(II)	$H_2P_2O_7^{2-}$, H_2O	$(Hdma)_2[Co(H_2P_2O_7)_2(H_2O)_2]$	[66]	DELNIS
8	Co(II)	$H_2P_2O_7^{2-}$, H_2O	$(Hetma)_2[Co(H_2P_2O_7)_2(H_2O)_2]$	[67]	SEMQEH
9	Co(II)	$HP_2O_7^{3-}$, H_2O	$(H_2en)_2[Co(HP_2O_7)_2(H_2O)_2]$	[68]	PEQZER
10	Ni(II)	$HP_2O_7^{3-}$, H_2O	$(H_2dap)_2[Ni(HP_2O_7)_2(H_2O)_2]\cdot 4H_2O$	[69]	FATZAC
11	Ni(II)	$HP_2O_7^{3-}$, H_2O	$H_2en[Cu(HP_2O_7)(en)(H_2O)]_2\cdot 2H_2O$	[68,70]	PEGLAP01, PEGLAP
12	Cu(II)	$HP_2O_7^{3-}$, H_2O, en	$(H_2en)[Cu(HP_2O_7)(en)(H_2O)]_2\cdot 2H_2O$	[72]	POKZOE
13	Cu(II)	$P_2O_7^{4-}$, H_2O, bipy	$\{[(bipy)Cu(H_2O)(\mu\text{-}P_2O_7)Na_2(H_2O)_6]\cdot 4H_2O\}$	[73]	XAXZEC
14	Pt(IV)	$P_2O_7^{4-}$, OH^-, NH_3	$\{[Pt(NH_3)_2(OH)_2(P_2O_7)Na_2(H_2O)_3]\cdot H_2O\}$	[17b]	–
15	Pt(IV)	$H_2P_2O_7^{2-}$, OH^-, en	$[Pt(en)(OH)_2(H_2P_2O_7)]$	[17b]	–
Dimers					
16	Cr(III)	$HP_2O_7^{3-}$, H_2O, NH_3	*fac*-$[Cr(HP_2O_7)(NH_3)_3]_2\cdot 2H_2O$	[61]	–
17	Co(III)	$P_2O_7^{4-}$, tpa	$\{[Co(tpa)_2]_2(\mu\text{-}P_2O_7)\}(ClO_4)_2\cdot 2.5CH_3OH\cdot 2.5H_2O$	[76]	QAXJAB
18	Mn(II)	$P_2O_7^{4-}$, phen	$\{[Mn(phen)_2]_2(\mu\text{-}P_2O_7)\cdot 13H_2O\}$	[10]	NILDES
19	Co(II)	$P_2O_7^{4-}$, phen	$\{[Co(phen)_2]_2(\mu\text{-}P_2O_7)\cdot 6MeOH\}$	[11]	SODVOX
20	Ni(II)	$P_2O_7^{4-}$, phen	$\{[Ni(phen)_2]_2(\mu\text{-}P_2O_7)\cdot 27H_2O\}$	[10]	NILDIW
21	Cu(II)	$P_2O_7^{4-}$, bipy, H_2O	$\{[Cu(bipy)(H_2O)]_2(\mu\text{-}P_2O_7)\cdot 7H_2O\}$	[12]	QIWDOP
22	Cu(II)	$P_2O_7^{4-}$, phen, H_2O	$\{[Cu(phen)(H_2O)]_2(\mu\text{-}P_2O_7)\cdot 8H_2O\}$	[18]	–
23	Cu(II)	$HP_2O_7^{2-}$, bipy, Cl^-	$\{[Cu(bipy)]_2(\mu\text{-}HP_2O_7)(\mu\text{-}Cl)\}\cdot H_2O$	[13]	–
24[a]	Zn(II)	$P_2O_7^{4-}$, L_1	$\{[(L_1\cdot 2Zn(\mu\text{-}P_2O_7)][K(H_2O)_3]\cdot 3H_2O\}$	[77]	EJOGUF
25[b]	Zn(II)	$P_2O_7^{4-}$, L_2	$\{[(L_2\cdot 2Zn(\mu\text{-}P_2O_7)][Na_2Li(CH_3CN)_2(CH_3OH)_5\text{-}(H_2O)_4]\cdot 7CH_3CN\cdot 5CH_3OH\cdot 2H_2O\}$	[78]	LIPRUY
26	Pt(II)	$P_2O_7^{4-}$, chd	$\{[Pt^{II}(chd)]_2(\mu\text{-}P_2O_7)\}\cdot 4H_2O$	[17b]	–
Tetramers					
27	VO(II)	$P_2O_7^{4-}$, CH_3O^-	$(Htmp)_4[(VO)_4(\mu\text{-}P_2O_7)_2(\mu\text{-}OCH_3)_4]$	[55]	NEJCOU
28	VO(II)	$P_2O_7^{4-}$, CH_3O^-	$(Hdma\text{-}dmn)_4[(VO)_4(\mu\text{-}P_2O_7)_2(\mu\text{-}OCH_3)_4]\cdot CH_3OH\cdot PhCH_3$	[55]	NEJDAH
29[c]	Cu(II)	$P_2O_7^{4-}$, L_3	$[(CuL_3)_4(P_2O_7)]\cdot nH_2O$	[14]	KITSOH
30	Cu(II)	$P_2O_7^{4-}$, bpa, H_2O	$\{[(bpa)Cu(H_2O)(\mu\text{-}P_2O_7)Cu(bpa)]_2\cdot 9H_2O\}$	[15]	SITZUP
31	Zn(II)	$P_2O_7^{4-}$, bipy, H_2O	$\{[(bipy)Zn(H_2O)(\mu\text{-}P_2O_7)Zn(bipy)]_2\cdot 14H_2O\}$	[73]	XAXZIG
Hexamers					
32	Cu(II)	$P_2O_7^{4-}$, NPY, CH_3CN, H_2O	$[(NPY)_6Cu_6(CH_3CN)_2(H_2O)_4(P_2O_7)_2](ClO_4)_4$	[80]	–
Polymers (3D)					
33	Co(II)	$P_2O_7^{4-}$, bpym	$\{[Co_2(\mu\text{-}P_2O_7)(bpym)_2]\cdot 5H_2O\}_n$	[16]	–

[a] L_1 = [μ_2-4-(2-(4-nitrobenzene)azo)-2,6-bis(*N*,*N*-bis(2-pyridylmethyl)aminomethyl)phenolato].
[b] L_2 = [μ_2-2,6-bis(bis((6-acetamidopyridin-2-yl)methyl)amino-methyl)phenolato].
[c] L_3 = 2-formylpyridine thiosemicarbazone; n = 9–12.

One of the major difficulties in attaining new pyrophosphate-containing coordination compounds [10,11] as well as solid-state structures [64] has been the anion's strong sensitivity to hydrolysis, especially in the presence of divalent metal ions. Other factors such as the extremely poor solubility of the anion in non-aqueous solvents or a significant sensitivity to the pH of the solution for the incorporation of the ligand into the complex [13] can be evoked as well.

This small number of examples however provides a wealth of exciting and diverse structural motifs, as well as highly significant physical properties. The crystal structures of the monomeric (**1**–**12** and **15**, containing transition metal ions only) or pseudo-monomeric (**13** and **14**, supported by Na^+ cations), as well as the higher-nuclearity complexes (dimers, tetramers, hexamers and polymers, **16**–**33**) reported to date are listed in Table 1, and will be discussed here. For a separate schematic representation of the principal counterions/co-ligands present in the reported structures see Fig. 4 and for interested readers, selected solid-state structure have been collected in Table 2, although further description of their crystal structures and properties goes beyond the scope of this review.

The attractiveness of PPi as a ligand is clear looking at the assortment of coordination modes that have been observed in the small number of coordination compounds reported to date. All these coordination modes are illustrated in Fig. 5, including a collection of unique coordination modes adopted by PPi in selected solid-state polymers (see Table 2).

2.1. Monomers

2.1.1. Chromium(III)

Chromium(III)–pyrophosphate coordination complexes have attracted considerable attention in the past as models for metal–nucleotide substrates for the investigation of enzyme activity, thanks to the inert character of the metal ion respect to Mg(II), which is the normal metal cofactor *in vivo* [63]. In the 1980s Sundaralingam et al. succeeded in the isolation and crystallization of five monomeric Cr(III)–pyrophosphate analogues, the compounds of formula $[Cr(HP_2O_7)(NH_3)_4]\cdot 2H_2O$ (**1**), *mer*-$[Cr(HP_2O_7)(NH_3)_3(H_2O)]\cdot 2H_2O$ (**2**), $[Cr(HP_2O_7)(NH_3)_2(H_2O)_2]\cdot nH_2O$ [with n = 1 (**3**) or 2 (**4**)], and $[Cr(HP_2O_7)(H_2O)_4]\cdot 3H_2O$ (**5**) (see Fig. 6). The number of coordinated H_2O or NH_3 molecules was modified by the authors to examine changes in enzyme activity, hydrolysis and recognition [60,63]. These complexes were prepared by the reaction of the appropriate Cr(III) (containing the desired number of ammonia and/or water molecules) and pyrophosphate (either $H_2Na_2P_2O_7$ or $Na_4P_2O_7$) salts at low pH (2–3), to ensure the partial protonation of the anion and the molecular electroneutrality. As shown in Fig. 6,

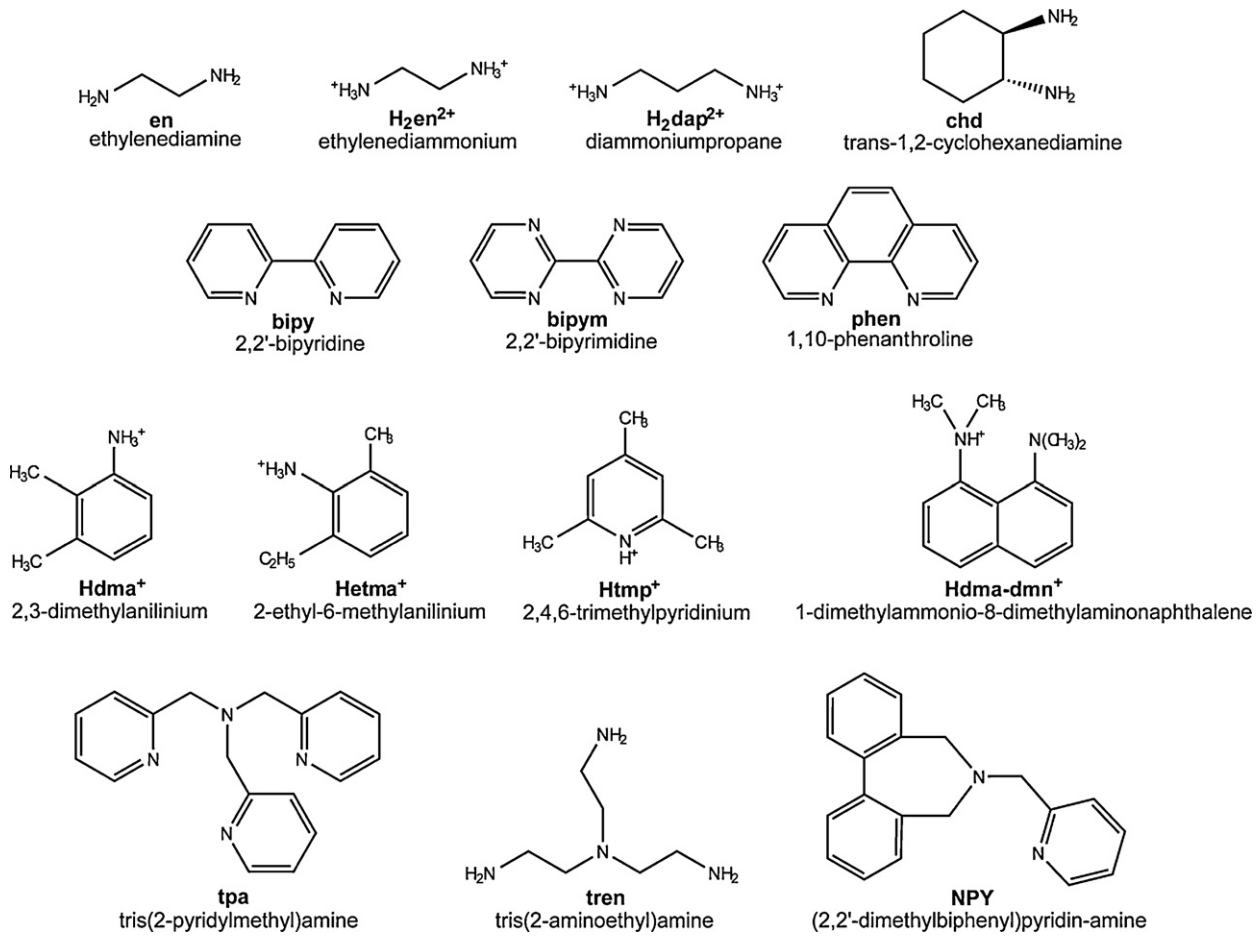

Fig. 4. Principal counterions and co-ligands present in the structurally characterized pyrophosphate-containing compounds listed in Table 2.

Table 2
Selected structurally characterized solid-state structures featuring the pyrophosphate ligand.[a].

Compound	Metal ion	Ligands	Molecular formula	References	CCD code
Organometallic					
34[b]	Ti-Co	$P_2O_7^{4-}$, O^{2-}, L_{OEt}^{-}	$[(L_{OEt}Ti)_2(\mu\text{-}O)(\mu\text{-}P_2O_7)]\cdot 5H_2O$	[81]	NEDDAC
Polyoxometallates					
35	W(VI)	$P_2O_7^{4-}$, O^{2-}	$Cs_{13}Na_3[(P_2O_7)_4W_{12}O_{36}]\cdot 24H_2O$	[82]	–
36	Mo(VI)	$P_2O_7^{4-}$, O^{2-}	$(NBu_4)_4[(P_2O_7)Mo_{18}O_{54}]$	[83]	–
37	Mo(VI)	$P_2O_7^{4-}$, O^{2-}	$(NBu_4)_4[(P_2O_7)Mo_{18}O_{54}](NBu_4)_2H_9[\{(P_2O_7)Mo_{15}O_{45}\}_2][PMo_{12}O_{40}]$	[64]	–
38	Mo(VI)	$P_2O_7^{4-}$, O^{2-}, H_2O	$(NMe_3Ph)_4[(P_2O_7)Mo_6O_{18}(H_2O)_4]\cdot 4H_2O$	[84]	MAPVAA
39	Mo(V)	$P_2O_7^{4-}$, CH_3COO^{-}, O^{2-}, H_2O	$Na_{24}[Na_4(H_2O)_6\{(Mo_2O_4)_{10}(P_2O_7)_{10}(CH_3COO)_8(H_2O)_4\}\cdot 97H_2O$	[85]	PACDUT
40	Mo(V)	$P_2O_7^{4-}$, $HCOO^{-}$, O^{2-}	$Na_{28}[Na_2\{(Mo_2O_4)10(P_2O_7)_{10}(HCOO)_{10}\}]\cdot 108H_2O$	[86]	YAWKUD
41	Mo(V)	$P_2O_7^{4-}$, CH_3COO^{-}, O^{2-}, H_2O	$Na_{22}(H_3O)_2[Na_4\{(Mo_2O_4)_{10}(P_2O_7)_{10}(CH_3COO)_8(H_2O)_4\}]\cdot 91H_2O$	[87]	YAWLAK
1D polymers					
42	V(III)	$P_2O_7^{4-}$, $H_2PO_4^{-}$	$\{(H_2en)[V(\mu\text{-}P_2O_7)(\mu\text{-}H_2PO_4)]\}_n$	[88]	QATNOO
43	Fe(III)	$H_2P_2O_7^{2-}$, $H_2PO_4^{-}$	$\{[Fe(\mu\text{-}P_2O_7)(\mu\text{-}H_2PO_4)]\cdot py\}_n$	[89]	OFICAI
44	Ni(II)	$HP_2O_7^{3-}$, F^{-}	$\{(H_2en)_2[Ni_2(HP_2O_7)_2(\mu\text{-}F)_2]\}_n$	[90]	XORCAI
45	Ga(III)	$P_2O_7^{4-}$, $H_2PO_4^{-}$	$\{(H_2dap)[Ga(\mu\text{-}P_2O_7)(\mu\text{-}H_2PO_4)]\}_n$	[91]	FACMOM
46	Ga(III)	$P_2O_7^{4-}$, F^{-}	$\{(H_2dap)[Ga(\mu\text{-}P_2O_7)(\mu\text{-}F)]\cdot 3H_2O\}_n$	[92]	MINWEL, MINWEL01
47	Ga(III)	$P_2O_7^{4-}$	$\{(H_2dap)[Ga(\mu\text{-}P_2O_7)(\mu\text{-}F)]\cdot H_2O\}_n$	[93]	MINWIP, MINWIP01
48	Ga(III)	$P_2O_7^{4-}$	$\{(H_2en)[Ga(\mu\text{-}P_2O_7)(\mu\text{-}H_2PO_4)]\}_n$	[88]	QATNII
2D polymers					
49	Cr(II)	$P_2O_7^{4-}$	$\{Na_2Cr(P_2O_7)\cdot 0.5H_2O\}n$	[93]	SITZUP
50	Eu(III)	$HP_2O_7^{3-}$, H_2O	$\{[Eu_2(H_2O)_4(HP_2O_7)_2]\cdot en\}_n$	[94]	PIBZAC
51	Tb(III)	$HP_2O_7^{3-}$, H_2O	$\{[Tb_2(H_2O)_4(HP_2O_7)_2]\cdot en\}_n$	[94]	PIBYUV
52	Er(III)	$HP_2O_7^{3-}$, H_2O	$\{[Er_2(H_2O)_4(HP_2O_7)_2]\cdot en\}_n$	[94]	PIBYOP
3D polymers					
53	V(III), VO(II)	$P_2O_7^{4-}$	$\{V_2(VO)(\mu\text{-}P_2O_7)\}_n$	[95]	GAWGUG
54	VO(II)	$P_2O_7^{4-}$	$\{(VO)_2(\mu\text{-}P_2O_7)\}_n$	[46]	–

[a] An overview of some pyrophosphate salts can be found in [83b] and references therein.
[b] L_{OEt}^{-} = Klaüi's tripodal ligand $[CpCo\{P(O)(OEt)_2\}_3]^{-}$, where Cp = η_5-C_5H_5.

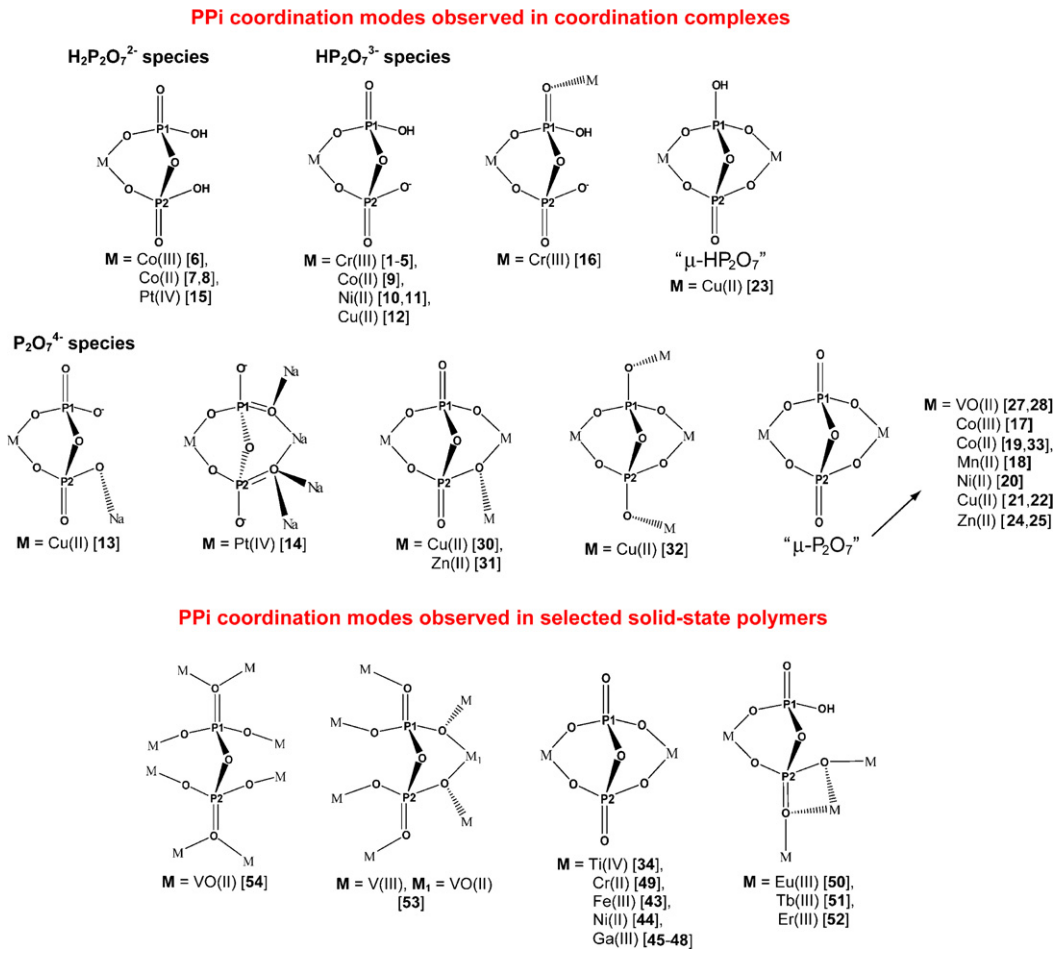

Fig. 5. Coordination modes adopted by the PPi ligand that have been observed to date. The numbers in brackets refer to the compounds as they have been listed in Tables 1 and 2.

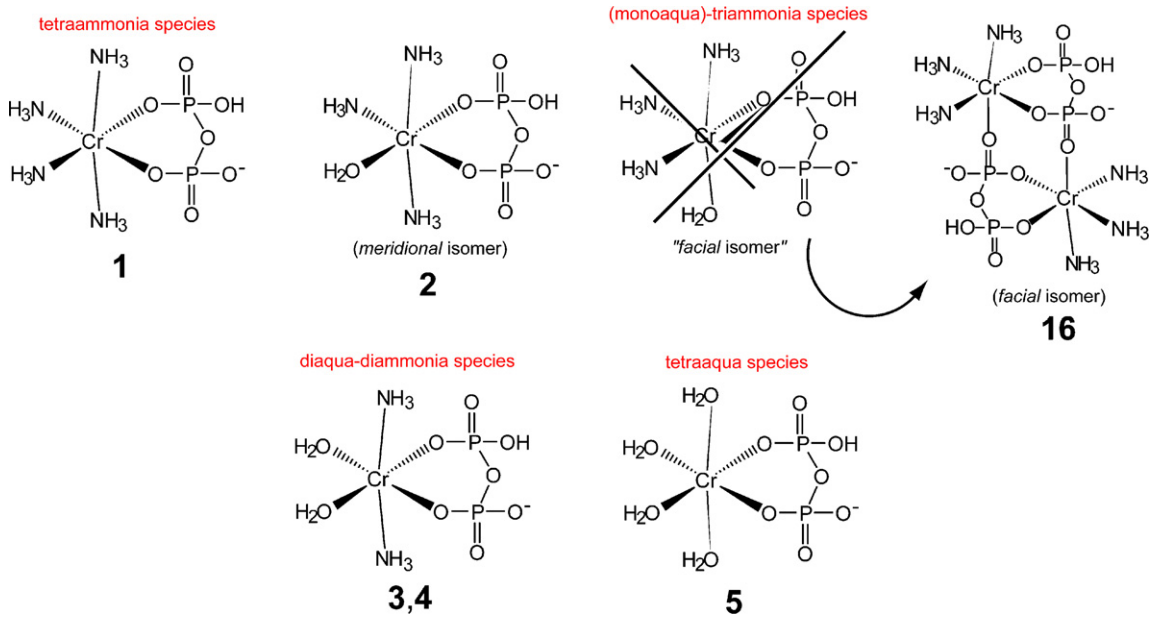

Fig. 6. Schematic representation of compound **1**–**5** [60–63]. Note that the *fac* isomer of **2** has not been isolated, the water molecule in the axial position being replaced by a pyrophosphate oxygen atom in order to form the dimeric species **16** [61] (see Section 2.2.1).

Table 3
Selected crystallographic data and structural features for the chromium(III)–pyrophosphate complexes **1**–**5** and **16**.

	1 [60]	**2** [61]	**3** [62]	**4** [62]	**5** [63]	**16** [61]
Formula	$H_{17}CrN_4O_9P_2$	$H_{16}CrN_3O_{10}P_2$	$H_{13}CrNO_{10}P_2$	$H_{15}CrNO_{11}P_2$	$H_{15}CrO_{14}P_2$	$H_{24}Cr_2N_6O_{16}P_4$
Crystal system	Monoclinic	Monoclinic	Triclinic	Monoclinic	Triclinic	Monoclinic
Structural features[a]						
Cr– O_{pyr}(eq)/Å	1.968(2)	1.945(3)	1.94(1)	1.93(1)	1.951(3)	1.951(3)
Cr–O_{pyr}(ax)/Å	N/A	N/A	N/A	N/A	N/A	1.969(3)
Cr–O_w/Å	N/A	1.993(3)	2.001(8)	1.998(3)	1.971(3)	N/A
Cr–NH_3/Å	2.07(1)	2.056(2)	2.04(1)	2.07(1)	N/A	2.048(4)
O–Cr–O/°[b]	90.1(1)	91.8(3)	90.3(3)	90.2(3)	91.9(1)	91.5(3)
Cr–O–P/°	127.5(1)–128.3(1)	135.4(5)–136.5(5)	128.8(2)–129.3(2)	137.6(2)	125.9(2)–132.7(2)	137.1(3)–136.1(3)
P–O–P/°	128.1(1)	129.5(3)	128.0(3)	136.6(3)	126.9(2)	135.0(3)
Ring puckering profile[c]						
Q/Å	0.62	0.37	0.56	0.097	0.58	0.23
θ/°	88.8	71	93.1	–	96.2	100
φ/°	104.3	169	119.3	–	306.7	10

[a] Average values reported, except for the bridging P–O–P angle, which is unique due to the presence of a single pyrophosphate anion in these complexes.
[b] Value of the pyrophosphate bite angle.
[c] Cremer–Pople parameters.

both the *meridional* and *facial* isomers of the aquatriammonia species have been characterized, with the latter exhibiting a dimeric structure with formula *fac*-$[Cr(HP_2O_7)(NH_3)_3]_2{\cdot}4H_2O$ (**16**, see Section 2.2). Selected crystallographic details and structural features for **1**–**5** and **16** have been collected in Table 3.

In all examples, the chromium(III) ion is in an octahedral environment, and the pyrophosphate ligand coordinates in a bidentate manner (Fig. 7), a coordination mode necessary for enzyme recognition of the trivalent metal ion [61,62].

The six-membered ring derived from the chelation of PPi to the metal ion always adopts a boat conformation as pointed out by the authors by using the Cremer–Pople formalism [65] (see Table 4). The greatest puckering is observed in the tetraammonia complex **1** (Q = 0.62 Å), while the PPi-coordination chelate ring in the dihydrate form **4** is essentially planar with a puckering amplitude of only 0.097 Å.

Since these complexes are all neutral, their crystal packing is essentially governed by an extensive network of intermolecular hydrogen bonds, involving the monomeric units as well as the water molecules of crystallization. In the case of compounds **1** and **3**, intramolecular hydrogen bonds between the axial ammonia ligands and pyrophosphate oxygen atoms can also be detected.

While these compounds are structurally similar, there are considerable differences in the chromium and pyrophosphate coordination environment (see select bond lengths and angles in Table 3). Significant changes are observed in the average angle attended at the coordinated pyrophosphate oxygen atom (Cr–O–P). In the tetraammonia compound **1** (Fig. 7a), this angle is ∼128° [range 127.5–128.2°], while in the tetraaqua compound **5** (Fig. 7b) the corresponding two angles are distinctly different, with values of 126° and 133°. The mono-**3** and dihydrate complexes **4** again show

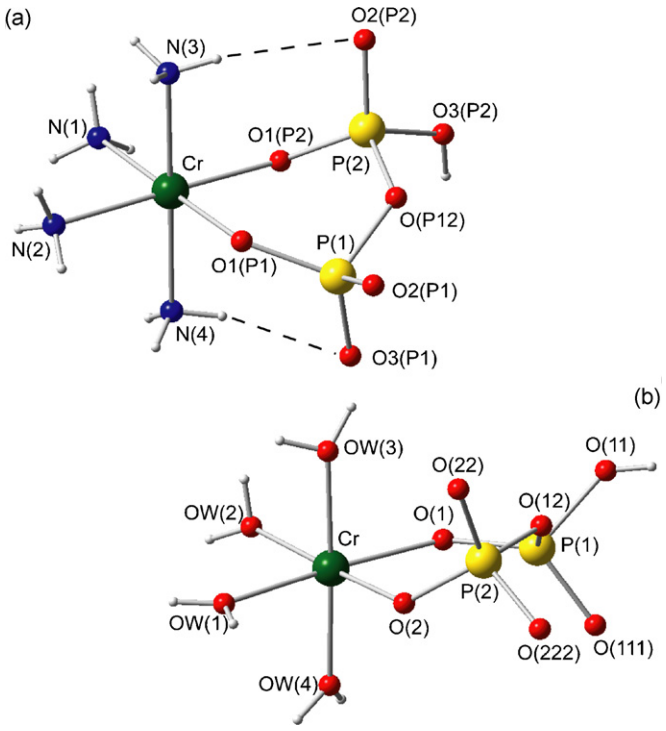

Fig. 7. Molecular structure of (a) $[Cr(HP_2O_7)(NH_3)_4]{\cdot}2H_2O$ (**1**)[60], showing the intramolecular hydrogen bonds between the ammonia ligand and the PPi oxygen atom, and (b) $[Cr(HP_2O_7)(H_2O)_4]{\cdot}3H_2O$ (**5**) [63], with the original labelling scheme.

Table 4
Selected crystallographic data and structural features for the mononuclear cobalt(II)– and nickel(II)–pyrophosphate complexes **7**–**11**.

	7 [66]	**8** [67]	**9** [68]	**10** [69]	**11** [70]
Formula	$C_{16}H_{32}CoNO_{16}P_4$	$C_{18}H_{36}CoN_2O_{16}P_4$	$C_4H_{26}CoN_4O_{16}P_4$	$C_6H_{38}NiN_4O_{20}P_4$	$C_4H_{26}NiN_4O_{16}P_4$
Crystal system	Triclinic	Triclinic	Triclinic	Triclinic	Triclinic
Structural features[a]					
M–O_{pyr}/Å	2.062(2)	2.069[b]	2.091[b]	2.057(1)	2.058(2)
M–O_w/Å	2.151(2)	2.144[b]	2.133[b]	2.116(1)	2.107(2)
O–M–O/°[c]	90.33[b]	89.78[b]	92.87[b]	94.37(4)	93.33(6)
P–O–P/°	129.05(6)	130.44[b]	129.84[b]	129.95(7)	129.16(1)

[a] Average values reported.
[b] Standard deviation not available.
[c] Value of the pyrophosphate bite angle.

a large contrast in their Cr–O–P angles exhibiting values of 129° and 138°, respectively. The aquatriaammonia complex **2** shows an average angle of 136° which is very similar to that found in **4** (138°) possibly due to the presence of two lattice water molecules in both complexes. The authors speculated that more water molecules present in the structure, the more intricate the network of hydrogen bonds, resulting in the flattening of the chelate ring. The incorporation of both coordinated and free-lattice water molecules going from **1** to **5** seems to affect also the Cr–O_{pyr} bond distance, as exemplified by the tetraammonia (**1**) and the tetraaqua (**5**) complexes, with average bonds of 1.97 and 1.95 Å, respectively. The shorter bond of 1.93 Å is observed in **4** (possessing a total of four water molecules in the asymmetric unit). The presence/degree of a hydrogen-bonding network plays a key role in defining this trend.

Of note, investigation of the enzymatic activity of these complexes revealed that the presence of coordinated water molecules improves the enzyme recognition. All these species were recognized by pyrophosphatases, but the tetraaqua complex **5** was hydrolyzed with greater efficiency, exhibiting a hydrolysis rate 20 times faster than its parent tetraammonia compound. This may be attributed to the ability of the coordinated water molecules to accept hydrogen bond donation from the enzyme [63].

2.1.2. Cobalt(II/III) and nickel(II)

A series of monomeric pyrophosphate coordination complexes of cobalt(II) and nickel(II), the compounds of formula $(Hdma)_2[Co(H_2P_2O_7)_2(H_2O)_2]$ (**7**) [66] $(Hetma)_2[Co(H_2P_2O_7)_2(H_2O)_2]$ (**8**) [67] $[H_2en]_2[Co(HP_2O_7)_2(H_2O)_2]$ (**9**) [68] $(H_2dap)_2[Ni(HP_2O_7)_2(H_2O)_2]\cdot 4H_2O$ (**10**) [69] and $(H_2en)_2[Ni(HP_2O_7)_2(H_2O)_2]$ (**11**) [70] has been recently reported (see Table 4 for selected crystallographic and structural data of **7**–**11**). A cobalt(III) monomer of formula $[Co(H_2P_2O_7)(tren)]ClO_4\cdot H_2O$ (**6**) is known instead from the late 1989 [71]. These complexes have been obtained by the stoichiometric reaction of a cobalt/nickel salt with pyrophosphoric acid ($H_4P_2O_7$) and a base[tris(2-aminoethyl)amine in **6**, 2,3-dimethylaniline in **7**, 2-ethyl-6-methylaniline in **8**, ethylenediamine in **9** and **11** and propanediamine in **10**]. All these compounds can be classified as molecular salts, being the metallo-pyrophosphate complexes either cationic (in **6**) or anionic (in **7**–**11**) species.

The cationic unit of **6** consists of a dihydrogenpyrophosphate ($H_2P_2O_7^{2-}$) Co(III) complex [note that all the previous discussed, neutral chromium(III) ones have been isolated with the pyrophosphate ligand in its monoprotonated state]. As shown in Fig. 8, the cobalt(III) is in an octahedral environment, its coordination sphere completed by a tetradentate, tris-chelating tris(2-aminoethyl)amine ligand (tren). The electroneutrality of the complex is completed by a perchlorate ion.

Compounds **7**–**11** are significantly different from **6** as well as the already cited Cr(III) examples, the stoichiometry of the complex being no longer 1:1, but 1:2 (metal to 2 PPi ligand per 1 metal ion). Indeed, this peculiar feature makes **7**–**11** unique among all the monomeric species listed in Table 1, increasing their attractiveness as potential building-blocks for the construction of high-dimensional pyrophosphate coordination compounds.

The pyrophosphate ligand in **7**–**11** again coordinates in a bidentate fashion (see Fig. 9). The Co(II) or Ni(II) octahedral coordination sphere is completed by two *trans*-water molecule ("axial" direction). The resulting $[M(H_xP_2O_7)_2(H_2O)_2]^{-(8-2x)+2}$ unit (with M = Co(II) for **7**–**9** and Ni(II) for **10**–**11**) has a di- or tetraanionic character, depending on the presence of PPi in its di- (**7**–**8**) or monoprotonated (**9**–**11**) state, respectively.

In the crystal packing of all these complexes, the anionic units and the countercations form two separate domains (see Fig. 10b and c), held together essentially by electrostatic forces. Weak π–π interactions are observed in the cationic domain when the countercation is an aromatic group (compounds **7** and **8**).

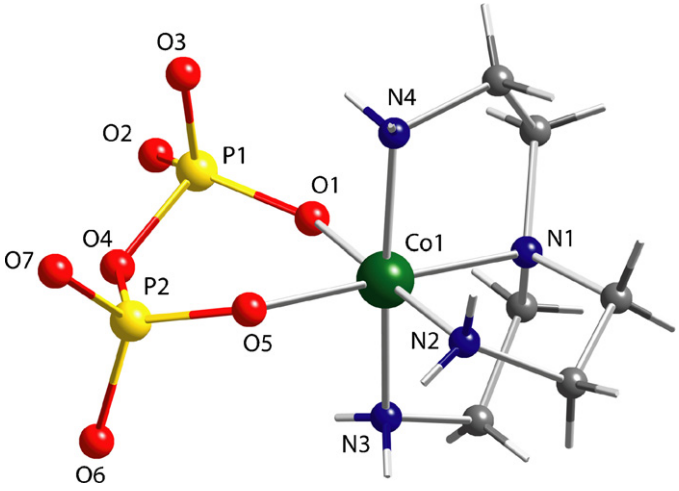

Fig. 8. Molecular structure of the cationic $[Co(H_2P_2O_7)(tren)]^+$ unit in **6**, with the original labelling scheme (hydrogen atoms on the $H_2P_2O_7^{2-}$ ligand not found) [71].

The M^{II} octahedra are connected *via* an extensive network of hydrogen bonds involving the pyrophosphate anions and the coordinated water molecule, which creates anionic layers in the *ab* plane (Fig. 10).

2.1.3. Copper(II)

As shown listed in Table 1, there are currently two copper(II) monomers reported to date, the compounds of formula $H_2en[Cu(HP_2O_7)(en)(H_2O)]_2\cdot 2H_2O$ (**12**) [72] and $\{[(bipy)Cu(H_2O)(P_2O_7)Na_2(H_2O)_6]\cdot 4H_2O\}$ (**13**) [73] (selected crystallographic and structural data are reported in Table 5).

The metal environment in these systems is very similar, the metal ion being coordinated in both cases to one pyrophosphate group ($HP_2O_7^{3-}$ in **12** and $P_2O_7^{4-}$ in **13**), a nitrogen capping ligand (ethylenediamine in **12** or bipyridine in **13**, see Fig. 11), and a water molecule occupying the apical position of the distorted

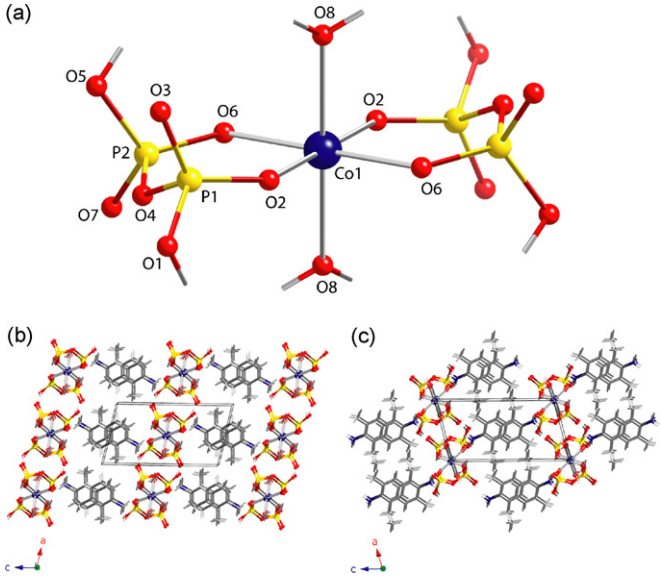

Fig. 9. (a) Molecular structure of the dianionic $[Co(H_2P_2O_7)_2(H_2O)_2]^{2-}$ centrosymmetric unit in **7** [66] and **8** [67] with the original labelling scheme, and respective crystal packing ((b) and (c)). Please note that the tetraanionic $[M(HP_2O_7)_2(H_2O)_2]^{4-}$ unit in **9** (M = Co(II)) and **10**–**11** (M = Ni(II)) is very similar, the only difference being the degree of protonation of the PPi ligand [68–70].

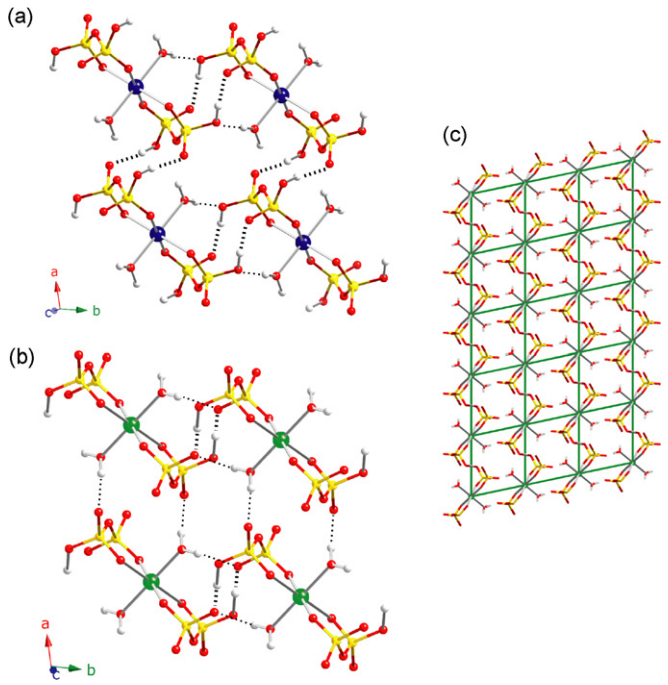

Fig. 10. Hydrogen bonding interactions connecting the anionic units in compounds **7**–**11**, evidencing the different profile in the presence of the dihydrogen- (a) or monohydrogen- (b) pyrophosphate species. (c) A view of the layer generated by these hydrogen bonds in **7**–**11**, highlighting the metal ions' connectivity.

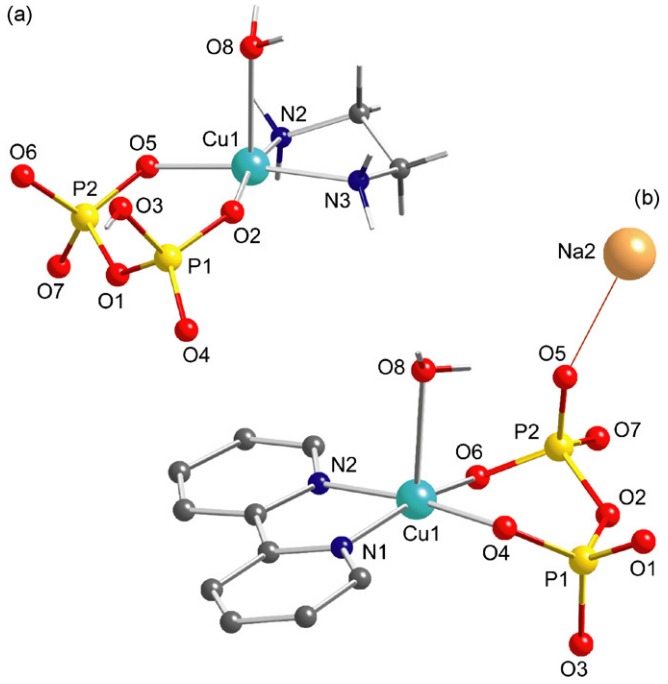

Fig. 11. Molecular structure of (a) the monoanionic $[Cu(HP_2O_7)(en)(H_2O)]^-$ unit in compound **12** [72] and (b) the dianionic $[(bipy)Cu(H_2O)(P_2O_7)]^{2-}$ unit in compound **13** [73] showing one of the two crystallographically independent Na^+ cations necessary to achieve the electroneutrality (note that the required second Na^+ cation is not directly coordinated to the pyrophosphate ligand, see text). The hydrogen atoms on the bipy ligand in **13** are not shown.

square pyramidal geometry [the trigonality parameter $\tau = 0.02$ for **12** and 0.15 for **13**] [74]. On the other hand, the geometry of the coordinated pyrophosphate group its quite different, varying in the value of the dihedral angle between the two condensed PO_4 tetrahedra. This value is close to 0° [average value ~9°] in **12** but close to 60° [average value ~46°] in **13**. Of note here, while the ligand shows a rather perfect (accidental or symmetry-imposed) eclipsed conformation in the majority of the known compounds, a marked staggered one is not so common. In fact, it has been observed in **13** as well as in other five complexes only (four mononuclear and one tetranuclear), as illustrated in Fig. 12. In any case, this distortion can be rationalized taking into consideration the presence of strong hydrogen bonds involving the hydrogen-pyrophosphate anion (compounds **1**, **3** and **6**) or an expanded coordination environment of the tetranionic species (that is tri-, hexa- and tetra-coordinated in **13**, **15** and **29**, respectively).

The diverse degree of deprotonation of the PPi group in **12** and **13** accounts for the different nuclearity of these two complex. In fact, even if both compounds are monomeric complexes, **13** is better described as a polymeric (2D) species from a structural point of view, the charge of the fully deprotonated pyrophosphate anion in this compound being neutralized through sodium cations that actively participate in the construction of a higher dimensionality framework.

Curiously, **12** has been obtained starting from copper(II) hydroxocarbonate, en and pyrophosphoric acid in slight excess of base, while **13** has been achieved from an aqueous solution of $Cu(OH)_2$, bipy and $Na_4P_2O_7$ in a stoichiometric 1:1:1 molar ratio. The tri- or tetraanionic character of the pyrophosphate group in **12** and **13** respectively, appears thus to be a direct consequence of the completely different strategies adopted in synthesizing these two complexes.

Table 5
Selected crystallographic data and structural features for the copper(II)–pyrophosphate complexes **12** and **13**.

	12 [72]	**13** [73]
Formula	$C_6H_{34}Cu_2N_6O_{17}P_4$	$C_{10}H_{30}CuN_2Na_2O_{18}P_2$
Crystal system	Monoclinic	Triclinic
Structural features[a]		
Cu–O_{pyr}/Å	1.957(2)	1.929(2)
Cu–O_w/Å	2.342(2)	2.312(2)
Cu–N/Å	2.006(2)	2.000(1)
O–Cu–O/°[b]	94.29[c]	93.92(7)
P–O–P/°	128.6(1)	126.1(1)

[a] Average values reported for the Cu–O_{pyr} and Cu–N bond distances.
[b] Value of the pyrophosphate bite angle.
[c] Standard deviation not available.

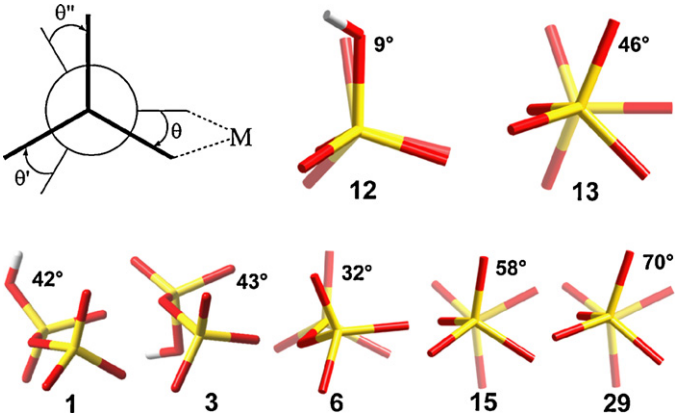

Fig. 12. View of the geometry of the pyrophosphate anion in selected compounds with the average dihedral angle values (see scheme on the left). *Up line*: anion conformation in **12** and **13**. Please note that the eclipsed conformation in **12** is the most common among the structurally characterized pyrophosphate compounds reported to date. *Bottom line*: the anion adopts a marked staggered conformation only in other four monomeric compounds (**1** [60], **3** [62], **6** [71] and **15** [17b]) and in the tetrameric complex **29** [15].

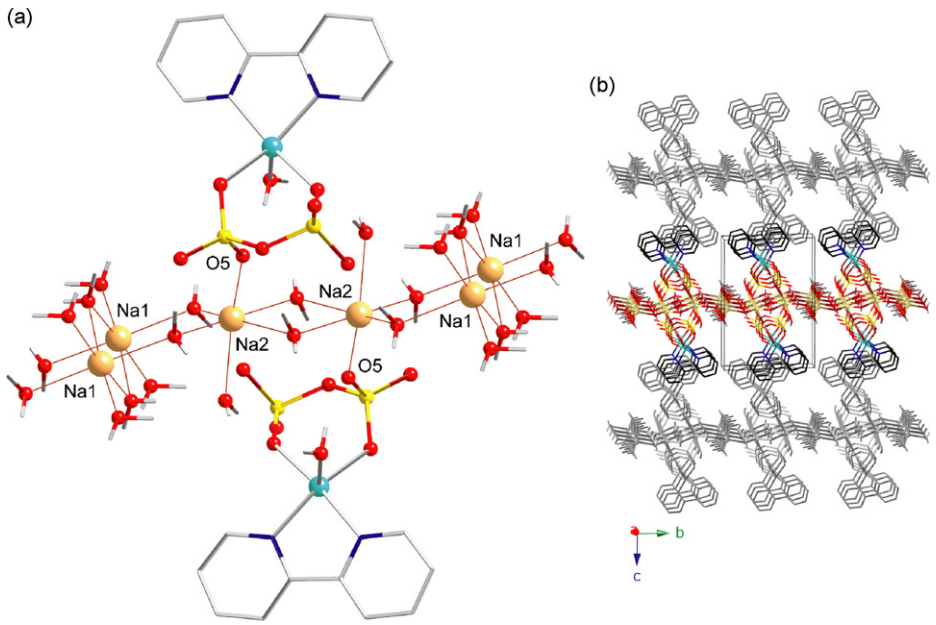

Fig. 13. (a) View of a fragment of the crystal packing of **13** [73] highlighting the Na–H_2O motif in the *ab* plane and anchored $[(bipy)Cu(H_2O)(\mu\text{-}P_2O_7)]^{2-}$ units; (b) view of the crystal packing of **13**, showing the stacking of the layers (or *tapes*) in the direction of the crystallographic *c* axis.

Looking at the crystal packing, compound **12** consists of monoanionic $[Cu(HP_2O_7)(en)(H_2O)]^-$ units and ethylenediammonium (H_2en^{2+}) cations held together by electrostatic forces and hydrogen bonds in which also the water molecule of crystallization are naturally involved.

Intermolecular N–H···O type bonds between the coordinated en ligand and one of the coordinated pyrophosphate oxygen atom (O2) result in the formation of $[Cu(HP_2O_7)(en)(H_2O)]^-$ layers, with the free water molecules and the H_2en^{2+} cations residing in between.

As already mentioned, the crystal packing of **13** is directed by additional sodium–pyrophosphate as well as by sodium–water bonds. As shown by Fig. 13a, the two required Na^+ cations (both six-coordinated) are involved in the formation of extensive and ornate Na–H_2O sheets parallel to the crystallographic *ab* plane. The dianionic $[(bipy)Cu(H_2O)(P_2O_7)]^{2-}$ units are anchored to these layers through the Na2 ions, which coordinate the pyrophosphate O5 oxygen atom. Alternate units, linked to adjacent Na2 ions, contribute to separate the sodium–water sheets by a distance corresponding to the entire *c* axis length (~16 Å), being disposed above and below them. The overall H_2O–Na-$[(P_2O_7)Cu(H_2O)(bipy)]$ layers stack along the *a* axis, interacting through the pending bipy ligands (see Fig. 13b). This arrangement results in the formation of channels, which in turn host the water molecules of crystallization.

2.1.4. Platinum(IV)

A series of pyrophosphate-platinum(II) and platinum(IV) coordination complexes has been recently synthesized and *in solution*-characterized by Bose and co-workers [17b] with the aim to explore their potentiality as chemotherapeutics (see Section 4).

The Pt(II) compounds have been synthesized starting from a water solution of an appropriate *cis*-diamminedichloro salt [cisplatin, dichloro(ethylenediamine)platinum(II) or *cis*-dichloro(*trans*-1,2-cyclohexanediamine)platinum(II)] and sodium pyrophosphate. The Pt(IV) complexes have been prepared following the same methodology, upon oxidation of the metal ion by 30% H_2O_2.

Of the six studied mononuclear compounds (three for each platinum oxidation state), two Pt(IV) complexes, of formula $\{[Pt(NH_3)_2(OH)_2(P_2O_7)Na_2(H_2O)_3]\cdot H_2O\}$ (**14**) and $[Pt(en)(OH)_2(H_2P_2O_7)]$ (**15**), have been successfully crystallized and analyzed through single-crystal X-ray diffractometry. A seventh compound, which has been obtained directly in the solid crystalline state from a water/DMF diffusion, has been characterized as the dinuclear Pt(II) complex $\{[Pt^{II}(chd)]_2(\mu\text{-}P_2O_7)\}\cdot 4H_2O$ (**26**) (see Section 2.2.6).

All these results appear quite relevant not only in the field of anti-cancer drug design, but also in the field of coordination chemistry. In fact, compounds **14**, **15** and **26** represent the only heavy-metal derivatives incorporating pyrophosphate whose crystal structures are known to date, with **26** being, in addition, the only one featuring the anion as bridging ligand.

Noticeably, the two Pt(IV) monomers **14** and **15** show a dissimilar chemical nature. This may be attributed either to the crystallization process or to the synthesis itself, even if the second hypothesis seems unlikely considering the same synthetic strategy adopted in the two cases.

This difference has to be related essentially to the nature of the PPi ligand, which is in its fully deprotonated form in **14**, while it exhibits diprotonation in **15**. Thus, for ensuring the electroneutrality of the solid phase, two sodium cations from the sodium pyrophosphate starting material are incorporated in the crystal packing of **14**, which turns to be, like the previous discussed copper(II) complex **13**, a structurally higher dimensionality species.

Here, both the two crystallographically independent Na^+ cations are coordinated to the pyrophosphate group. The incorporation of one hydroxyl group (O1) and three of the four water molecules of crystallization (O_{w2}–O_{w4}) into the coordination sphere of these two cations leads to the formation of $[(NH_3)_2Pt(OH)_2(P_2O_7)]$-Na–$H_2O$ *tapes* growing in the direction of the *a* axis. As shown in Fig. 14, this motif is completely different from the one observed in **13**, not only because of the different dimensionality (1D in **14** *vs.* 2D in **13**), but especially because of the pyrophosphate anion denticity. A single pyrophosphate oxygen atom links a single sodium cation in **13** whereas two different O_{pyr} atoms link two (O8) or even three (O6) sodium cations at once in **14**. The occurrence of this μ_3-oxygen atom is responsible for the formation of the quasi-cubane 1D arrangement of Na^+ cations illustrated by Fig. 14c [75].

As shown if Fig. 15, no sodium atoms necessitate to be included in the crystal structure of compound **15**, since the electroneutrality of the complex is already ensured by the presence of a

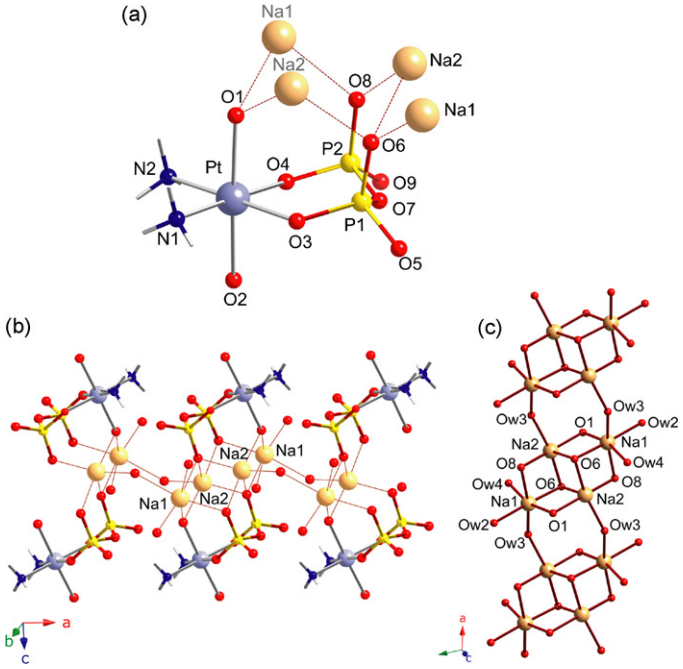

Fig. 14. (a) Molecular structure of the dianionic $[Pt(NH_3)_2(OH)_2(P_2O_7)]^{2-}$ unit in compound **14** [17b] with the original labelling scheme, also showing the way the two crystallographically independent Na^+ cations necessary to achieve the electroneutrality are coordinated to the pyrophosphate ligand; (b) a view of the $[(NH_3)_2Pt(OH)_2(P_2O_7)]$-Na–$H_2O$ *tapes* growing in the direction of the *a* axis in **14**, with the quasi-cubane Na–O motif highlighted in (c).

dianionic $H_2P_2O_7^{2-}$ bidentate species. Finally, the coordination environment of the platinum(IV) ion in both **14** and **15** is very similar, with no significant changes in the values of Pt-N [range 1.993(5)–2.017(5) Å] and Pt-O_{OH} [range 1.957(4)–2.044(4) Å] bond distances and main octahedral angles. Only the average Pt-O_{pyr} bond length appears slightly different, with a value of 2.024(4) Å in **14** *vs.* 2.048(5) Å in **15**, presumably due to some effects related to the presence/absence of the extra coordinated univalent sodium atoms.

The geometry of the pyrophosphate group is different too. In fact, even if the value of the bridging P–O–P angle is almost identical [128° in **14** vs. 126° in **15**], in **15** the anion adopts the unusual staggered conformation, with a dihedral angle of ~58° (see Fig. 12),

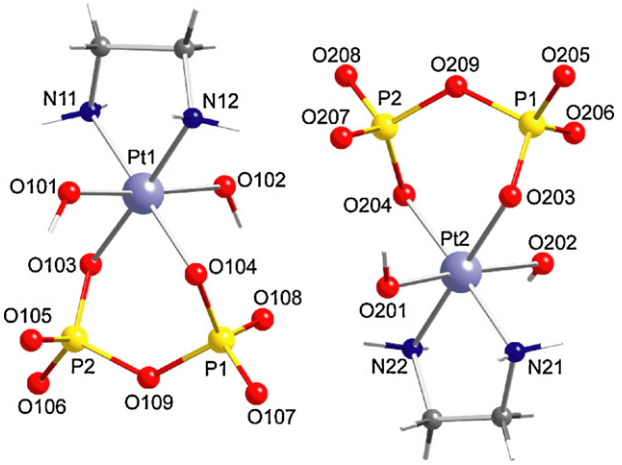

Fig. 15. A view of the two independent molecules in the asymmetric unit of the mononuclear Pt(IV) complex $[Pt(en)(OH)_2(H_2P_2O_7)]$ (**15**) [17b] with the original labelling scheme (hydrogen atoms on the $H_2P_2O_7^{2-}$ anion not located by the authors).

Table 6
Selected crystallographic data and structural features for the platinum–pyrophosphate complexes **14**, **15** and **26** [17b].

	14	**15**	**26**
Formula	$H_{16}PtN_2Na_2O_{13}P_2$	$C_2H_{12}PtN_2O_9P_2$	$C_{12}H_{25}Pt_2N_4O_{11}P_2$
Crystal system	Triclinic	Monoclinic	Triclinic
Structural features[a]			
Pt–O_{OH}/Å	2.005(4)	1.999(5)	N/A
Pt–N/Å	2.013(5)	2.008(5)	2.03(1)
O-Pt-O/°[b]	96.2(2)	90.7(2)	91.9(3)
P–O–P/°	127.9[c]	125.8[c]	125.3[c]

[a] Average values reported.
[b] Exact value (a single pyrophosphate group is present in the asymmetric unit of **14**).
[c] Standard deviation not available.

while in **14** the two fused PO_4 tetrahedra are almost perfectly eclipsed [average value for the dihedral angle less than 2°].

Another peculiarity of the structure of **15** is the occurrence of two crystallographic unique molecules in the asymmetric unit, with different chirality. As speculated by the authors, a truly enantiomeric relationship between these two units is prevented by the different orientation of the hydrogen atoms located on the *trans*-hydroxyl groups.

In both compounds, the crystal packing is directed essentially by the presence of extensive hydrogen bonds which involve the pyrophosphate anion, the ammine group (ammonia or en), the hydroxyl ions and the water molecules (in **14**). However, due to their different nature, the resultanting unit cells are in the two cases very different as well as the space group in which the two compounds crystallize (see Table 6).

2.2. Dimers

2.2.1. Chromium (III)

The structure of the dimeric chromium(III) complex of formula *fac*-$[Cr(HP_2O_7)(NH_3)_3]_2{\cdot}4H_2O$ (**16**) reported by Sundaralingam et al. in the 1990 [61] consists of two $[Cr(HP_2O_7)(NH_3)_3]$ units connected *via* a rare double O–P–O bridge (Fig. 16). These units are related by a centre of inversion and the chromium coordina-

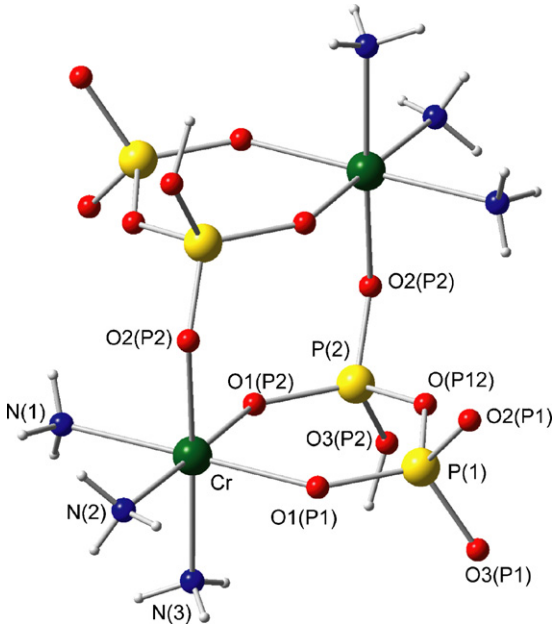

Fig. 16. Molecular structure of the chromium(III)–pyrophosphate complex in *fac*-$[Cr(HP_2O_7)(NH_3)_3]_2{\cdot}4H_2O$ (**16**), with the original labelling scheme [61].

tion environment is identical to that of the previously discussed mononuclear chromium systems (selected crystallographic details and structural parameters for **16** have been collected in Table 4).

As already mentioned in Section 2.1.1, this complex can be considered as the *facial* isomer of the aquatriammonia species **2**, imagining the replacement of the axial water molecule with a pyrophosphate oxygen atom and the consequential fusion of two monomeric units (see Fig. 6).

As reported by the authors, the *mer*- and *fac*-isomer are always obtained together when mixing $[Cr(NH_3)_3(H_2O)Cl_2]Cl$ and $Na_2H_2P_2O_7$ in a 1:1 stoichiometric ratio. However, the isomer discussed here can be isolated only in a small amount (*fac*:*mer* isomeric molar ratio ~1:4), presumably due to the arrangement of the ammonia ligand in the chromium salt that is utilized as starting material. Even if the occurrence of different isomers can be also postulated for the diaquadiaammonia (complexes **3** and **4**) species, only the *cis*-aqua-*trans*-ammonia one (see Fig. 6) has been isolated so far [61,62]. Most likely, the existence of two so different (in shape and mass) isomers in the case of the aquatriammonia species makes it easier to detect and then separate them by chromatography [61].

From a structural point of view, no significant changes in the Cr–N and Cr–O_{pyr} bond distance and angles can be noted between the two isomers, excluding the Cr–O_2(P2) distance (see Fig. 16), which is somewhat longer [~.97 Å *vs.* an average value of ~1.95 and ~1.94 Å for the two standard chelating Cr–O_{pyr} bonds in **16** and **2**, respectively]. The most relevant features in the structure of **16** are related to the PPi group. The internal P–O–P angle is quite wider [135.0° *vs.* 129.5°] and the six-membered chelate ring upon coordination appears even flatter respect to **2**, presumably due to the dimer formation. The tridentate character of the $HP_2O_7^{3-}$ anion in **16** is rare and recalls in mind that of $P_2O_7^{4-}$ in the copper(II) complex **13**, being the coordination mode also very similar (see Fig. 5). However, the particular type of dinuclear arrangement in **16**, with special regards to the extra eight-membered ring formed between the two standard six-membered metallo-pyrophosphate chelate ones (see Fig. 6) remains pretty unique among the pyrophosphate coordination complexes known to date.

2.2.2. Cobalt(III)

Two crystallographic unique cobalt(III) metal centres linked by a bis-bidentate pyrophosphate [μ-pyrophosphato-$\kappa O^1O^2:\kappa O^3O^4$) group occur in the dimeric system $\{[Co(tpa)_2]_2(\mu\text{-}P_2O_7)\}(ClO_4)_2\cdot 2.5CH_3OH\cdot 2.5H_2O$ (**17**)[76] (Fig. 17). As in the cobalt(III) mononuclear species **6** [71] the cobalt atom in **17** is in an octahedral environment, its coordination sphere being completed by the tetradentate, tris-chelating tris(2-pyridylmethyl)amine (tpa, while it was tren in **6**). Again, the electroneutrality of the complex is ensured by the presence of perchlorate anions.

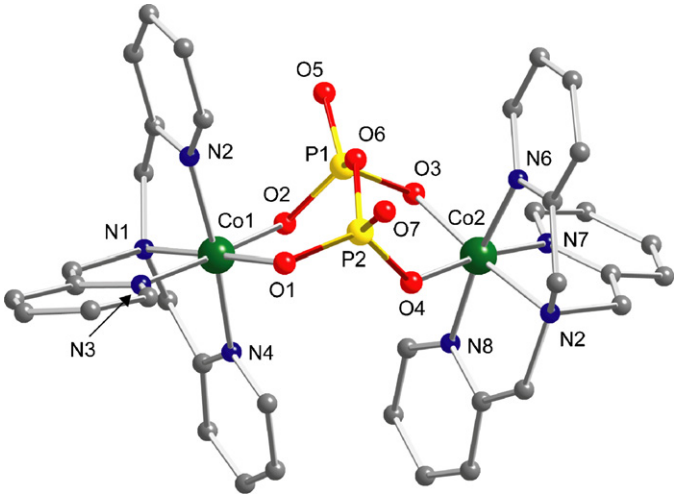

Fig. 17. Molecular structure of the dicationic $\{[Co(tpa)_2]_2(\mu\text{-}P_2O_7)\}^{2+}$ unit in **17**, with the original labelling scheme [hydrogen atoms on the tpa ligand are not shown] [76].

Curiously, the attainment of this complex did not derived from the interest in the exploration of the coordination chemistry of the pyrophosphate anion, being instead inspired by the lack of examples of phosphate–phosphate bond formation assisted by metal ions [76]. Thus, the isolation of **17** represents the success of the strategy adopted by the authors in pursuing this aim. In particular, the complex has been achieved in a very good yield mixing a Co(III)-tpa-carbonato species with two equivalents of disodium 4-nitrophenylphosphate in water, in presence of active charcoal. Any change in the optimized procedure (absence of charcoal, different phosphate source and pH value) has resulted not in a drop in the reaction yield but in the complete absence of the diphosphate species.

From a structural point of view, the dimer shape in **17** is totally different respect to that found in the previously discussed dinuclear chromium(III) species **16**. In fact, the pyrophosphate anion in **17** adopts the more frequent bis-bidentate, "μ" coordination mode (see Fig. 5). These same coordination mode and molecular shape have been observed in all the other dinuclear complexes known to date.

The values of the Co–N and Co–O bond distances in **17** are very similar to those found in the Co(III) monomer **6** [average values of 1.93 and 1.91 Å in **17** vs. 1.94 Å in **6**]. The two metal ions in the dimer are separated by ~4.95 Å. The crystal packing is facilitated by electrostatic forces, intermolecular π–π type interactions between the tpa ligands and hydrogen bonds involving the pyrophosphate ligand, the perchlorate anions and the free methanol and water molecules.

2.2.3. Manganese(II), cobalt(II) and nickel(II)

Three dimeric analogues of either manganese(II), cobalt(II) or nickel(II), $\{[Mn(phen)_2]_2(\mu\text{-}P_2O_7)\}\cdot 13H_2O$ (**18**) [10] $\{[Co(phen)_2]_2(\mu\text{-}P_2O_7)\}\cdot 6MeOH$ (**19**) [11] and $\{[Ni(phen)_2]_2(\mu\text{-}P_2O_7)\}\cdot 27H_2O$ (**20**) [10] have been recently reported by Doyle et al. The isolation of **18**–**20** is as a result of the systematic investigation of the pyrophosphate anion coordination chemistry began by the author in 2001 with the synthesis of the first complex incorporating the μ-P_2O_7 bridge, the compound of formula $\{[Cu(bipy)(H_2O)]_2(\mu\text{-}P_2O_7)\}\cdot 7H_2O$ (**19**) [12] which will be discussed in the next paragraph.

A schematic view of these complexes is presented in Fig. 18, while selected crystallographic and structural data are collected in Table 7.

In all these examples the dinuclear unit is made up of two crystallographically unique $[M(cis\text{-}phen)_2]^{2+}$ units bridged by the tetraanionic pyrophosphate ligand (see Fig. 18). The metal ion is

Table 7
Selected crystallographic data and structural features for the dimeric manganese(II)–, cobalt(II)– and nickel(II)–pyrophosphate complexes **18**–**20**.

	18 [10]	**19** [11]	**20** [10]
Formula	$C_{48}H_{58}Mn_2N_8O_{20}P_2$	$C_{54}H_{56}Co_2N_8O_{13}P_2$	$C_{49}H_{89}Ni_2N_8O_{34}P_2$
Crystal system	Triclinic	Triclinic	Tetragonal
Structural features[a]			
M–O_{pyr}/Å	2.105(3)	2.043(1)	2.057(8)
M–N/Å	2.301(4)	2.165(2)	2.15(1)
M···M/Å	4.700(1)	4.857(1)	5.031(1)
O–M–O/°	92.4(1)	94.27(5)	92.8(1)
P–O–P/°	125.9(2)	123.41(7)	124.8(5)

[a] Average values reported for the M–O_{pyr}/M–N bond distances and the pyrophosphate bite angle O–M–O.

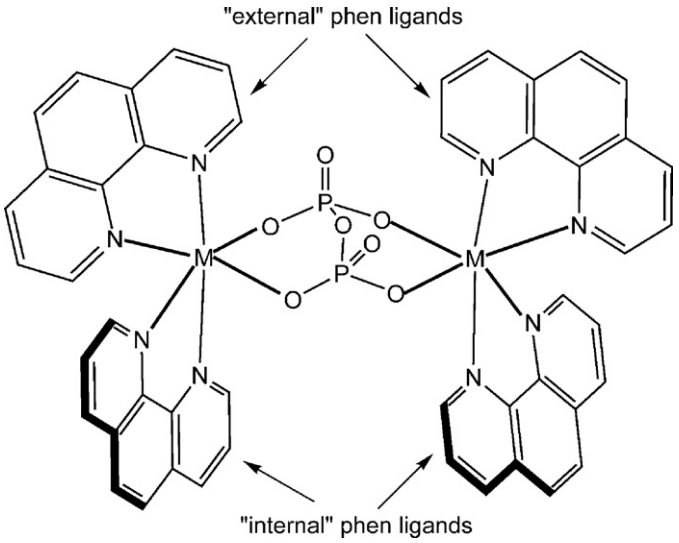

Fig. 18. Schematic representation of the dimeric analogues $\{[M(phen)_2]_2(\mu\text{-}P_2O_7)\}$ **18**–**20** [M = Mn(II) (**18**), Co(II) (**19**) and Ni(II) (**20**)] [10,11].

hexacoordinated, with four nitrogen atoms from two phen ligands and two pyrophosphate oxygen atoms building a distorted octahedral environment. The $P_2O_7^{4-}$ bridge separates the two metal centres by a distance going from ~4.70 in the manganese(II) dimer to ~5.03 Å in the nickel(II) one, with the value of the Co(II)···Co(II) separation residing in between (~4.86 Å). This unexpected trend does not follow the observed, natural shortening of the metal–O_{pyr} bond when passing from Mn(II) to Ni(II) (note that the Co– and Ni–O_{pyr} bond distances are practically comparable, see Table 7), but can be explained taking in consideration the distortion imposed on the dinuclear unit by the stronger intradimer π–π interaction involving the two "internal" phen ligands [interplanar separation of ~3.41, 3.36 and 3.23 Å in **18**, **19** and **20**, respectively]. Such distortion of the metal environment is also reflected in the pyrophosphate anion shape, with the value of the average dihedral angle between the two fused PO_4 tetrahedra increasing from ~18° to 24° when passing from **18** to **20** [being ~21° in **19**].

Despite these small differences, the dinuclear $\{[M(phen)_2]_2(\mu\text{-}P_2O_7)\}$ unit in **18**–**20** can be considered isostructural. Strong packing analogies can be found however only between **18** and **19**, while **20** crystallizes in a remarkably different way.

Compounds **18** and **19** both crystallize in the triclinic *P*1 space group, the unit cell dimensions varying slightly mostly due to the presence of 13 water molecules *vs*. six methanol molecules of crystallization in the Mn(II) and Co(II) analogues, respectively. Adjacent dimeric units interact through both the internal and external phen ligands, forming pseudo-layers parallel to the crystallographic (1 1 1) plane (see Fig. 19). In both structures, the solvent molecules of crystallization reside in and between these layers, participating in an extensive hydrogen-bonding network, which involves also the pyrophosphate oxygen atoms.

Surprisingly, compound **20** exhibits a supramolecular 3D open-framework, which constitutes a unique case among all the structurally characterized pyrophosphate compounds reported to date. Offset face-to-face and edge-to-face π–π interactions between the external phen ligands lead to the formation of two types of channels, differing in size and nature, running down the crystallographic *c*-axis (see Fig. 20). As noted by the author, the character of the biggest one (type A) is predominantly hydrophobic, being this channel defined by phen ligands which project aromatic C–H group into it, while the other one (type B) is clearly hydrophilic, being principally delineated by pyrophosphate anions whose oxygen atoms are involved in extensive hydrogen bonds as usual. However, due to their large dimension (17.813 Å × 17.813 Å), disordered crystallization water molecules can be also found in the type A channels (Fig. 20). Indeed, the Ni(II) complex has the highest solvent occupancy noted to date (45.7% of the unit cell volume), which is almost twice that observed in **18** and **19** (26.4 and 26.1%, respectively).

The magnetic properties of compound **18**–**20** have been analyzed by the authors as part of their ongoing interest in the systematic magneto-structural investigation of pyrophosphate-bridged transition metal complexes [10,11] and will be discussed in Section 3. More recently, the same authors have undertaken the exploration of these systems as potential drugs/prodrugs. Compounds **19** and **20** have been tested in adriamycin-resistant human ovarian cancer cell line (A2780/AD), with **19** resulting in picomolar cytotoxicity at 72 h (the same analysis on compound **18** has been precluded by solubility) [18]. Details on these results and recent developments in this promising research field will be furnished in Section 4.

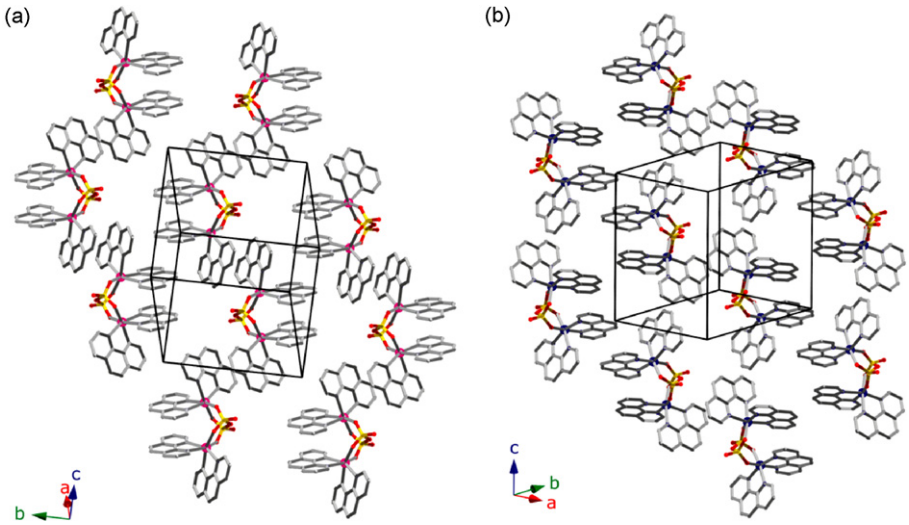

Fig. 19. View of the intra- and intermolecular π–π type interactions between the phen ligand in **17** (a) and **18** (b), leading in both cases to the formation of sheets growing in the crystallographic (1 1 1) plane. Hydrogen atoms on the phen ligand are not shown. Note that the intermolecular π–π stacking in **17** takes place along the *b*-axis (with the intramolecular one laying in the direction of the *ac*-plane diagonal) while a similar interaction in **18** occurs in the direction of the *ab*-plane diagonal (with the intra- one following the orientation of the dimeric unit along the *c*-axis).

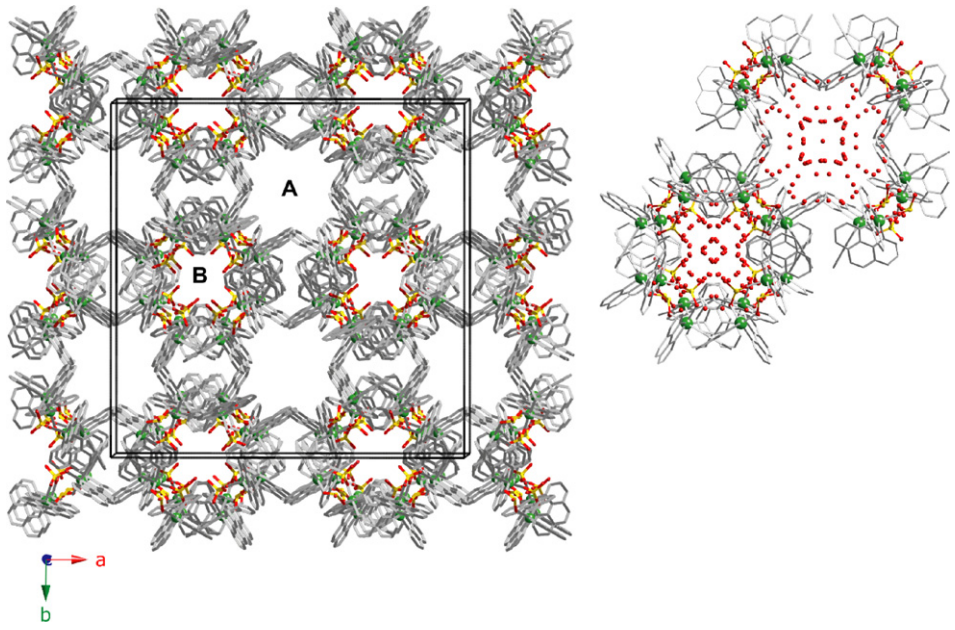

Fig. 20. *Left*: Packing diagram of **20** looking down the crystallographic *c*-axis, highlighting the porous supramolecular network generated by offset face-to-face and edge-to-face π–π interactions between the phen ligands (hydrogen atoms on the phen ligands and lattice water molecules not shown). The dimensions of the A and B channels are 17.813 Å × 17.813 Å and 13.163 Å × 15.71 Å, respectively. *Right*: Closeup showing the presence of free water molecules of crystallization inside both cavities, with a major density in the B channels due to its strong hydrophilic character.

2.2.4. Copper(II)

Three copper(II)–pyrophosphate dimeric complexes have been reported to date, the compound of formula $\{[Cu(bipy)(H_2O)]_2(\mu\text{-}P_2O_7)\}\cdot 7H_2O$ (**21**) being, as already mentioned, the first one among all the known structures showing the incorporation of a bis-bidentate $P_2O_7^{4-}$ ligand (Fig. 21a). This compound was isolated and characterized by Doyle and co-workers in 2001 [12] and can be considered the archetype of all the modern $P_2O_7^{4-}$ bridged complexes. The compounds of formula $\{[Cu(phen)(H_2O)]_2(\mu\text{-}P_2O_7)\}\cdot 8H_2O$ (**22**) [18] and $\{[Cu(bipy)]_2(\mu\text{-}HP_2O_7)(\mu\text{-}Cl)\}\cdot H_2O$ (**23**, see Fig. 21b) [13] have been achieved more recently by the same authors, and they present only slight (case of compound **22**) or even significant (case of **23**) modifications respect to the original structure.

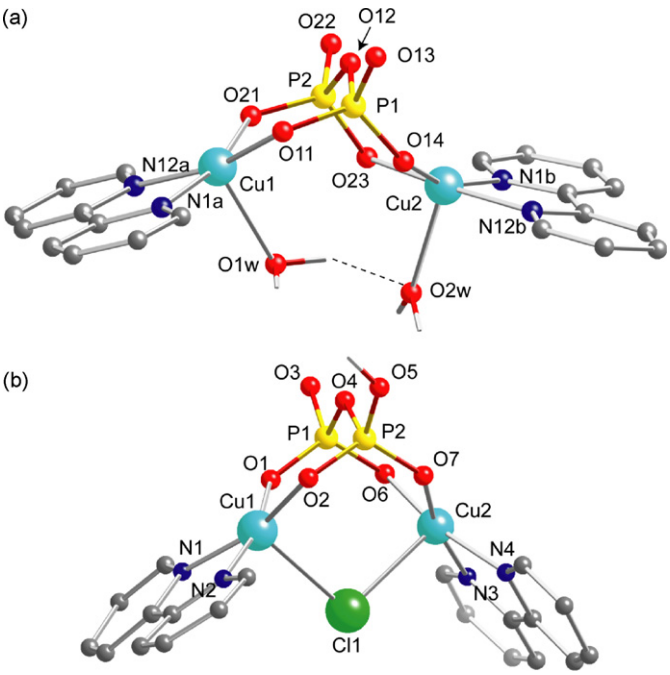

Fig. 21. Molecular structure of (a) $\{[Cu(bipy)(H_2O)]_2(\mu\text{-}P_2O_7)\}\cdot 7H_2O$ (**21**) [12] and (b) $\{[Cu(bipy)]_2(\mu\text{-}HP_2O_7)(\mu\text{-}Cl)\}\cdot H_2O$ (**23**) [13], with the original labelling scheme. The molecular structure of compound **22** is exactly analogous to that of **21** upon substitution of the bipy ligand with phen.

Compounds **21** and **22** have been prepared from the stoichiometric reaction, in water, of $Cu(OH)_2$ (or $Cu(NO_3)_2$), bipy (or phen) and sodium pyrophosphate [12,18] the same reaction led to the formation of **23** when the pH value of the solution was adjusted to ~8.5 with concentrated HCl/NaOH [13].

Compounds **21** and **22** are isomorphous (see crystallographic details in Table 8), the only difference in these two dimeric analogues being the nitrogen-capping ligand (bipy in **21** and phen in **22**) and the number of water molecules of crystallization (7 in **21** *vs.* 8 in **22**).

In both species, the copper(II) ions have a distorted square pyramidal geometry [average trigonality parameter $\tau \sim 0.1$ for **21** and **22**], with the basal plane defined by two bipy/phen nitrogen atoms [average Cu–N bond distances 2.015(5) Å] and two pyrophosphate oxygen atoms [with $Cu\text{–}O_{pyr} \sim 1.945(5)$ Å]. The remaining coordination site is occupied by an apical water molecule [$Cu\text{–}O_w$ bond lengths in the range 2.28–2.30 Å]. The dinuclear complex is thus made up of two crystallographically

Table 8
Selected crystallographic data and structural features for the dimeric copper(II)–pyrophosphate complexes **21**–**23**.

	21 [12]	**22** [18]	**23** [13]
Formula	$C_{20}H_{34}Cu_2N_4O_{16}P_2$	$C_{24}H_{36}Cu_2N_4O_{17}P_2$	$C_{20}H_{19}ClCu_2N_4O_8P_2$
Crystal system	Triclinic	Triclinic	Monoclinic
Structural features[a]			
$Cu\text{–}O_{pyr}$/Å	1.951(4)	1.935(5)	1.950(1)
$Cu\text{–}O_w$/Å	2.282(4)	2.296(5)	NA
Cu–N/Å	2.011(5)	2.018(6)	2.005(1)
Cu···Cu/Å	4.646	4.597	3.954
O–Cu–O/°	94.2(2)	95.3(2)	114.25(6)
P–O–P/°	121.4(2)	120.83(3)	121.11(7)

[a] Average values reported for the $Cu\text{–}O_{pyr}$, $Cu\text{–}O_w$ and Cu–N bond distances and for the pyrophosphate O–Cu–O bite angle.

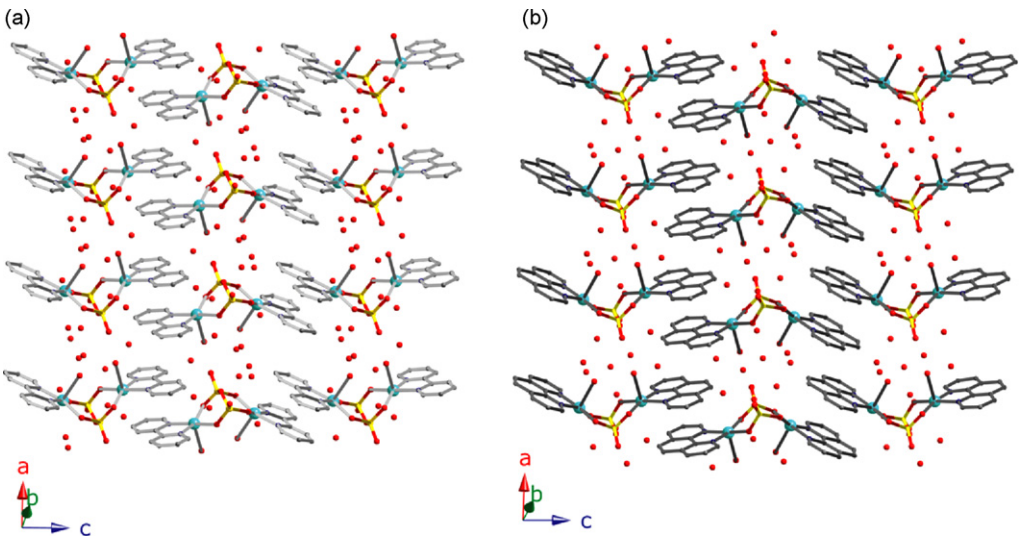

Fig. 22. View of a fragment of the crystal packing of (a) {[Cu(bipy)(H_2O)]$_2$(μ-P_2O_7)}·7H_2O (**21**) [12] and (b) {[Cu(phen)(H_2O)]$_2$(μ-P_2O_7)}·8H_2O (**22**) [18], showing the intermolecular π–π type interaction between the aromatic ligands (hydrogen atoms not shown for clarity).

unique [Cu(bipy/phen)(H_2O)]$^{2+}$ units linked by the bis-bidentate pyrophosphate bridge. As shown in Fig. 21a, the presence of an intramolecular hydrogen bond between the two apical water molecules imposes to the complex a rather distorted, asymmetric shape. This asymmetry becomes more evident looking at the pyrophosphate coordination environment. In fact, two different conformations of the six-membered chelate ring of the bis-bidentate pyrophosphate can be observed (chair at Cu1 and boat at Cu2).

Despite the slight difference in the lattice water contents, the two compounds show a very similar crystal packing (Fig. 22). A strong hydrogen bond involving a coordinated water molecule and a pyrophosphate oxygen atom [O2w···O13 = 2.77 Å (**21**) and O9w···O6 = 2.82 Å (**22**)] and intermolecular π–π type interactions between the bipy or phen ligands [with interlayer separation of 3.34–3.42 Å in **21** and 3.27–3.42 Å in **22**] both contribute to the formation of supramolecular 2D motif which grows parallel to the crystallographic *ac*-plane. These layers are hydrogen-bonded in the third direction *via* the free-lattice water molecules. These similarities transfer to the same unit cell parameters for **21** and **22**.

Given all these structural analogies, a similar magnetic behavior must also be expected for these two compounds. More important, compound **22** has been used in bio-comparative studies with the previously discussed phenanthroline-analogues **19** and **20** [10,11] with impressive results (see Section 4).

Conversely, the importance of the third compound of this series, the μ-$HP_2O_7^{3-}$/μ-Cl^- bridged species **23**, must be located in the field of magneto-chemistry. The attainment of this complex also testify the growing understanding of the coordination chemistry of the pyrophosphate ligand in the presence of transition metal ions which is essential for the ultimate goal of designing compounds with desired (or controllable) properties.

The dinuclear copper(II) complex in the case of **23** is made up of two crystallographically unique [Cu(bipy)]$^{2+}$ units linked by the bis-bidentate pyrophosphate and the additional single chloro bridge. Again, the metal ion exhibits a distorted square pyramidal geometry [average trigonal parameter $\tau \sim 0.08$], with the basal plane occupied by two bipy-nitrogen and two pyrophosphate oxygen atoms (Cu–O_{pyr} and Cu–N average bond lengths of ~1.95 and 2.01 Å, respectively, values which are very close to those found in **21** and **22**). The two independent copper(II) centres share a chloride anion, which occupies the apical position of both metal coordination spheres [with Cu–Cl bond lengths of 2.6267(5) and 2.6581(5) Å and a Cu–Cl–Cu angle of 96.86(4)°] [13].

The removal of one apical water molecule, and the substitution on the remaining one with a (bridging) Cl^- anion when ideally passing from **21** to **23**, causes a drastic consequence on the molecular shape, as highlighted by Fig. 21. In particular, the intradimer metal···metal separation passes from 4.646 Å in **21** to 3.954 Å in **23**, and the dihedral angle between the mean basal planes of the two copper(II) ions of the dimeric unit becomes 83.67 in **23**, being 132.8° in **21**. Also, the pyrophosphate six-membered chelate ring in **23** adopts a chair conformation at the Cu1 and Cu2 atoms. As a consequence, an increased molecular symmetry can be seen in **23** with respect to the single pyrophosphate-bridged species **21** and **22** [note that a real crystallographic relationship within the dimeric unit in **23** is prevented by the presence of the asymmetric $HP_2O_7^{3-}$ anion].

Compound **23** represents a unique case of a documented monohydrogenpyrophosphate-bridged complex (the previously discussed chromium(III) dimer **16** also contains $HP_2O_7^{3-}$ but in that case the anion does not adopt the bis-bidentate coordination mode) and a distinctive example of a double-bridged species, the pyrophosphate binding supported by an additional bridgehead chloride anion. The consequence of the incorporation of the additional bridge on the magnetic properties of the complex is discussed in Section 3.

2.2.5. Zinc(II)

A search in the Cambridge Structural Database (updated and reviewed in September 2009) reveals the occurrence of three zinc(II)-pyrophosphate species reported to date, two of them being dinuclear and the other one tetranuclear.

The binuclear complexes of formula {[(L_1·2Zn(μ-P_2O_7)][$K(H_2O)_3$]·3H_2O} (**24**) [77] and {[(L_2·2Zn(μ-P_2O_7)][$Na_2Li(CH_3CN)_2(CH_3OH)_5(H_2O)_4$]·7$CH_3CN$·5$CH_3OH$·2$H_2O$} (**25**) [78] [where L_1 = μ-4-(2-(4-nitrobenzene)azo)-2,6-bis(*N*,*N*-bis(2pyridylmethyl)aminomethyl)phenolato and L_2 = μ-2,6-bis(bis((6-acetamidopyridin-2-yl)methyl)aminomethyl)-phenolato], recently reported by Jong-In Hong et al., have been obtained upon recognition of the pyrophosphate anion in solution by a pre-formed Zn^{2+} complex (L_1·2Zn^{2+} in **24** and L_2·2Zn^{2+} in **25**, see Fig. 23).

In both **24** and **25** the pyrophosphate ligand adopts the bis-bidentate coordination mode, being the distorted octahedral

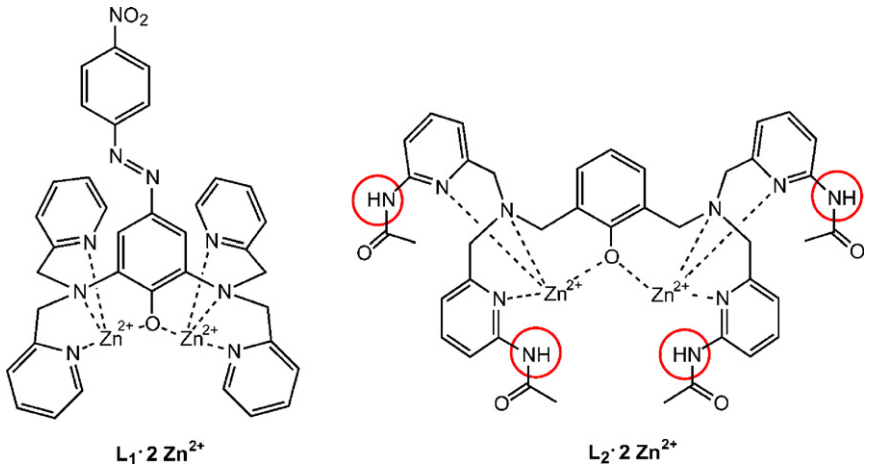

Fig. 23. Schematic representation of the two pyrophosphate receptors $L_1{\cdot}2Zn^{2+}$ [77] and $L_2{\cdot}2Zn^{2+}$ [78]. Note the presence of four N–H groups (hydrogen-bonding sites) on the L_2 ligand, which makes the $L_2{\cdot}2Zn^{2+}$ system a better PPi receptor respect to $L_1{\cdot}2Zn^{2+}$ and to the other PPi sensors reported to date, primarily based on metal coordination effects only [78].

environment of the zinc(II) ions completed by the multidentate ligands L_1 or L_2.

Of note, the structural characterization of **24**–**25** represents experimental evidence of the author's successful design of high-affinity/high-selectivity pyrophosphate receptors for the anions detection in solution. Both compounds in turn provide us with new patterns of pyrophosphate–alkaline metal ions interactions, enriching the variety of coordination modes already found in **13** and **14** (see Fig. 24).

2.2.6. Platinum(II)

As already mentioned in Section 2.1.4, a dinuclear pyrophosphate-platinum(II) complex has been lately isolated and structurally characterized by Bose and co-workers, the compound of formula $\{[Pt(chd)]_2(\mu\text{-}P_2O_7)\}{\cdot}4H_2O$ (**26**) [17b] which represents a rare example of heavy-metal derivative incorporating the bis-bidentate pyrophosphate bridge. Crystals of **26** have been obtained upon liquid-liquid diffusion of a concentrated aqueous solution containing the corresponding Pt(chd)-pyrophosphate monomer in DMF.

The coordination geometry around the two platinum(II) centres in **26** is almost perfectly square planar, as expected for the $5d^8$ electronic configuration. Two *cis*-nitrogen atoms from a cyclohexanediamine ligand and two *cis*-pyrophosphate oxygen atoms occupy the four sites of this square plane, showing very similar average Pt-N and Pt-O_{pyr} bond distances [~2.03(1) and 2.05(1) Å, respectively]. Moreover, the average values of the bite angle of the chd and $P_2O_7^{4-}$ ligands does not vary significantly from the theoretical value of 90° [being 83.9(4)° for the bidentate-chd and 91.9(3)° for the bis-bidentate pyrophosphate anion]. The Pt···Pt separation across the $P_2O_7^{4-}$ bridging group corresponds to ~3.37 Å, a value rather longer than the sum of two Pt covalent radii (1.30 Å in the Pauling scale). The steric hindrance of the non-aromatic chd ligand possibly accounts for this long Pt···Pt distance, causing the complex to assume a "V"-shape, with the two platinum(II) mean planes forming a dihedral angle of ~38°.

Adjacent dinuclear units are disposed in a zig-zag fashion, building a pseudo-···Pt···Pt···Pt···Pt··· chain running along the [−1 1 0] direction, with short (~3.237 Å) and long (~4.319 Å) interdimer Pt···Pt separations (see Fig. 25). An extensive network of hydro-

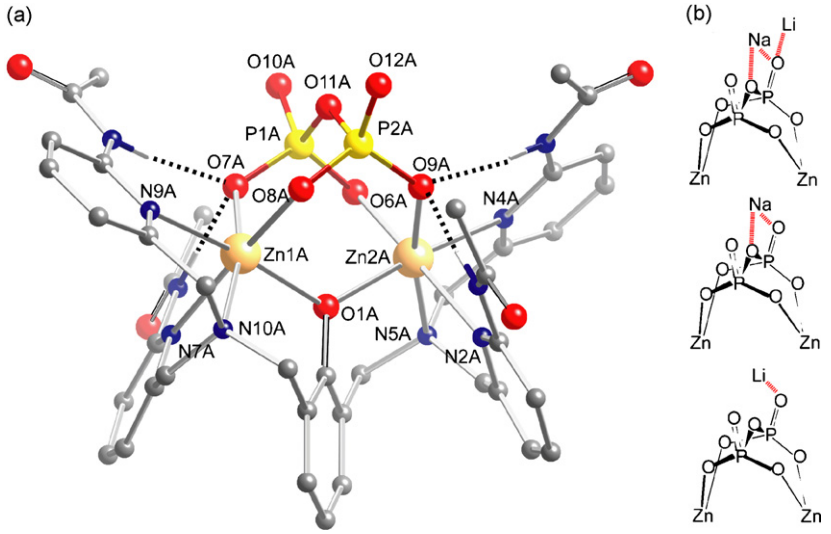

Fig. 24. (a) Molecular structure of one of the three isostructural monoanionic $[(L_2{\cdot}2Zn(\mu\text{-}P_2O_7)]^-$ dimeric molecules in the asymmetric unit of compound **25** [78], with the original labelling scheme. Note the presence of N–H···O_{pyr} contributing to anchor the pyrophosphate anion to the $L_2{\cdot}2Zn^{2+}$ sensor. (b) An overview of the complete coordination environment of the three independent pyrophosphate anions in **25**.

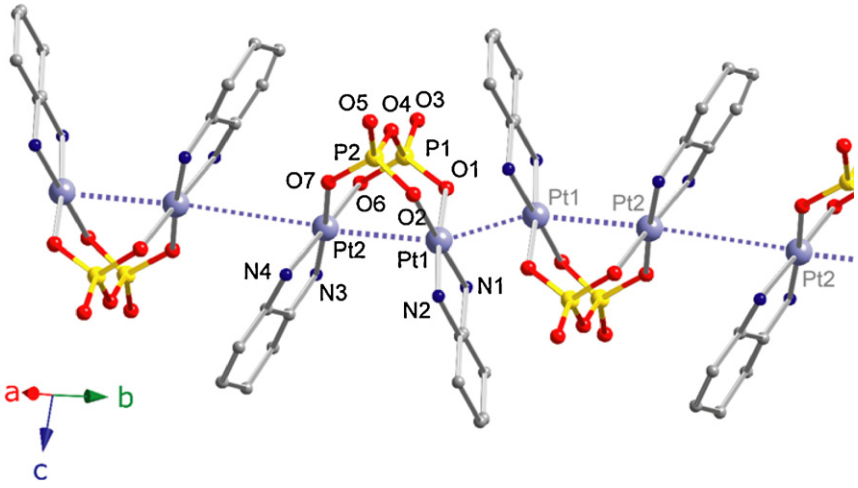

Fig. 25. 1D arrangement along the crystallographic [−1 1 0] direction of the neutral dinuclear $\{[Pt(chd)]_2(\mu\text{-}P_2O_7)\}$ units in **26** [17b] highlighting the intra- and intermolecular Pt···Pt short contacts: (*intra*) Pt1···Pt2 = 3.372 Å; (*inter*) Pt1···Pt1 = 3.237 Å; (*inter*) Pt2···Pt2 = 4.319 Å (hydrogen atoms on the chd ligands not shown).

gen bonds involving the four lattice water molecules and the pyrophosphate oxygen atoms ensure then the cohesion of these supramolecular chains in the three-dimensional structure.

2.3. Tetramers

2.3.1. Vanadyl [VO(IV)]

An unique example of discrete vanadyl-pyrophosphate species was reported by Herron et al. in 1997 [55]. These authors were able to isolate the compound of formula $(Htmp)_4[(VO)_4(\mu\text{-}P_2O_7)_2(\mu\text{-}OCH_3)_4]$ **27** by the reaction of vanadyl(IV) sulphate, pyrophosphoric acid and 2,4,6-trimethylpyridine, in methanol. Compound **27** was found to exhibit a very low solubility in methanol and other common organic solvents, presumably due to the presence of strong hydrogen bonds involving the vanadyl-pyrophosphate cluster and the trimethylpyridinium coutercations.

The metathesis of the $Htmp^+$ cation upon addition of excess 1,8-(dimethylamino)naphthalene in methanol/toluene resulted in the formation of the much more soluble analogue $(Hdma\text{-}dmn)_4[(VO)_4(\mu\text{-}P_2O_7)_2(\mu\text{-}OCH_3)_4]\cdot CH_3OH\cdot PhCH_3$ (**28**) (see selected crystallographic data and structural features in Table 9).

The isostructural, centrosymmetric $[(VO)_4(\mu\text{-}P_2O_7)_2(\mu\text{-}OCH_3)_4]^{4-}$ entity from **27** and **28** consists of four vanadyl (VO^{2+}) units connected by methoxo- and pyrophosphato-bridges. The vanadium ion, five-coordinated, adopts a distorted square pyramidal geometry, with the axial position defined by the V=O unit and the basal plane comprised of four oxygen atoms belonging to a bis-bidentate pyrophosphate group and two different μ-methoxo groups (Fig. 26).

Table 9
Selected crystallographic data and structural features for the tetrameric vanadyl compounds **27** and **28** [55].

	27	**28**
Formula	$C_{36}H_{60}V_4N_4O_{22}P_4$	$C_{78}H_{120}V_4N_8O_{26}P_4$
Crystal system	Monoclinic	Monoclinic
Structural features[a]		
V=O/Å	1.589	1.593
$V\text{–}O_{pyr}$/Å	1.954	1.957
V···V(pyr)/Å	4.718	4.508
V···V(MeO^-)/Å	3.125	3.133
O–V–O(pyr)/°	88.68	89.30
P–O–P/°	118.83	120.80

[a] Average values reported for the V=O and $V\text{–}O_{pyr}$ bond distances and the O–V–O pyrophosphate bite angle (standard deviation not available).

As in **27**, the crystal packing in **28** is governed by electrostatic forces and hydrogen bonds involving the pyrophosphate anion and the countercations, with the bigger $Hdma\text{-}dmn^+$ groups and the presence of additional solvent molecules of crystallization being reflected in a much lower density for **28** respect to **27** (1.33 g cm^{-3} *vs.* 1.55 g cm^{-3}).

Noteworthy, the isolation of a third vanadyl-pyrophosphate complex, with plausible formula $\{[VO(bipy)]_2(\mu\text{-}P_2O_7)\}\cdot 5H_2O$, has been reported by Doyle et al. more recently [73]. This compound has been obtained as microcrystalline powder by the reaction in water of $VOSO_4$ and bipy with sodium pyrophosphate, in a 2:2:1 molar ratio. The number of lattice waters has been estimated *via* TGA, while the proposed formula has been hypothesized on the basis of in-depth IR and magnetic analysis. However, the crystal structure of this complex is still needed to undoubtedly find out its nature and analyze its structural features in comparison with those of the VVP catalyst [73].

2.3.2. Copper(II) and zinc(II)

The complex of formula $[(CuL_3)_4(P_2O_7)]\cdot nH_2O$ (**29**) (where HL_3 = 2-formylpyridine thiosemicarbazone), was reported by Ain-

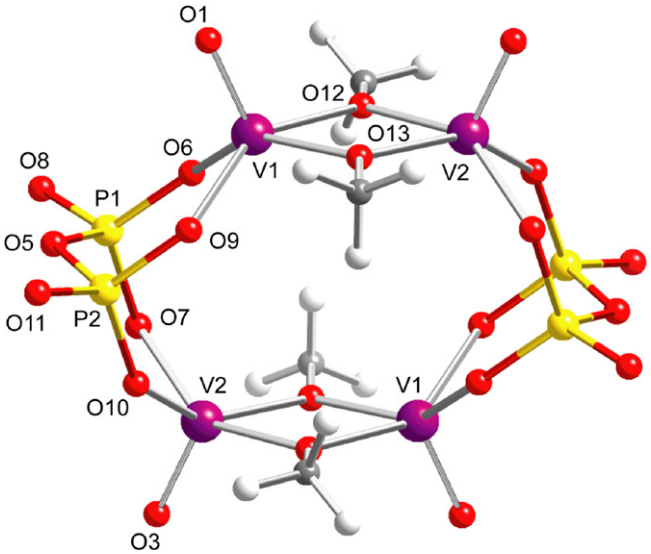

Fig. 26. Crystal structures of the isostructural $[(VO)_4(\mu\text{-}P_2O_7)_2(\mu\text{-}OCH_3)_4]^{4-}$ anionic core of **27** and **28**, with the original labelling scheme [55].

Table 10
Selected crystallographic data and structural features for the tetrameric copper(II) **29** and **30** and zinc(II) **31**.

	29[a] [14]	**30** [15]	**31** [73]
Formula	$C_{28}H_{46}Cu_4N_{16}O_{16}P_2S_4$	$C_{40}H_{58}Cu_4N_{12}O_{25}P_4$	$C_{40}H_{64}Zn_4N_8O_{30}P_4$
Crystal system	Monoclinic	Monoclinic	Monoclinic
Structural features[b]			
M–O_{pyr}(eq)/Å	1.90(1)	1.91(1)	1.967(2)
M–O_{pyr}(ax)/Å	N/A	2.256(6)	2.166(2)
M–O_w/Å	N/A	2.516[c]	2.017(2)
M–N/Å	1.98(1)	1.93(1)	2.109(3)
O–M–O/°	N/A	89.1, 92.9[c]	89.9(1), 97.2(1)
P–O–P/°	132.9(4)	121.72	125.21[c]

[a] Data for $n = 9$.
[b] Average values reported.
[c] Standard deviation not available.

scough et al. in 1992 as the product of the reaction in water of the acetate–precursor complex $[CuL_3(CH_3COO)]_2$ with $Na_4P_2O_7$, in the stoichiometric 1:2 molar ratio [14]. The crystallization water content was found to vary within the sample so that $n = 9$–12 (see crystallographic details in Table 10). A schematic representation of the thiosemicarbazonato ligand is showed in Fig. 27a, together with the coordination mode adopted by the anion in complex **29**. It is clear that the geometry of the NNS^- donor set on this ligand perfectly fits with three of the four equatorial position in the copper(II) coordination sphere, leaving just one coordination site free for the pyrophosphate attach. The tetrakismonodentate bridging mode exhibited by the PPi group in **29** is different from the more common bis-bidentate coordination mode, and it still remains unique among the structure reported to date.

As shown in Fig. 27, each copper(II) ion in **29** is five-coordinated in a distorted square pyramidal surrounding [the value of the trigonality parameter τ varies from 0.088 for Cu3 to 0.255 for Cu4]. The pyridine and amine nitrogen atoms as well as the negative charged thioamide sulphur of the thiosemicarbazonato ligand form two chelate rings upon coordination to the copper(II) ion, with the latter acting also as a bridge between two different metal centres. The two resulting $(CuL)_2^{2+}$ units are held together by the pyrophosphate group, which in this way builds the tetranuclear complex.

The Cu–N, Cu–S(equatorial), Cu–S(axial) and Cu–O_{pyr} bond distances vary in the ranges 1.920(7)–2.030(7), 2.2663–2.292(3), 2.852(3)–2.895(3) and 1.885(7)–1.916(7) Å respectively, these values being in agreement with the literature data [14]. The Cu···Cu distance across the double sulphur bridge is ~3.26 Å (average value), with the pyrophosphate group producing a much longer metal–metal separation [range 6.803–8.936 Å].

The PPi anion in this complex presents the greatest distortion from the ideal symmetric geometry noted to date, with a PO_3–PO_3 dihedral angle of ~70° and a O–P–O angle as large as 133°.

The great number of lattice water molecules traduces in the presence of an extensive network of hydrogen bonds all within the crystal, which can be evoked as the main factor that accounts for the stability of the three-dimensional structure. The stacking of the tetranuclear units along the *c*-axis, also stabilized by weak π–π

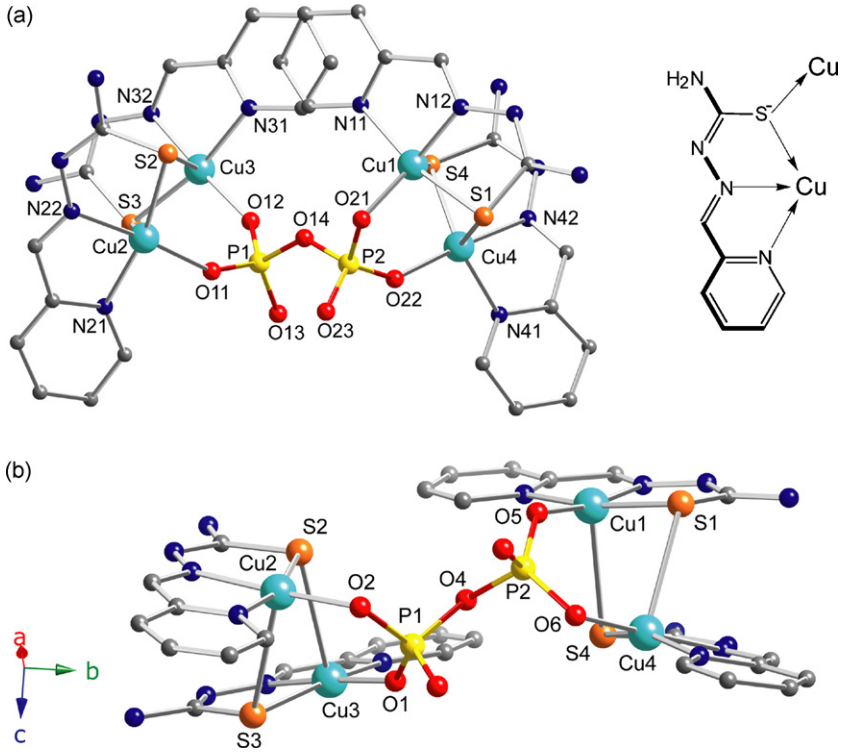

Fig. 27. Crystal structure of $[(CuL)_4(P_2O_7)]\cdot 9H_2O$ (**29**) [14] (water molecules of crystallization not shown). (a) *Left*: schematic representation of the thiosemicarbazone ligand emphasizing its coordination mode; *right*: top view of the complex. (b) A side view of the complex highlighting the copper(II) coordination environment. Note the possible magnetic pathways in **29**: (1) Cu–O–P–O–Cu (*syn–syn* phosphate bridge), (2) Cu–O–P–O–P–O–Cu (extended pyrophosphate bridge) and (3) Cu–S–Cu (equatorial-axial).

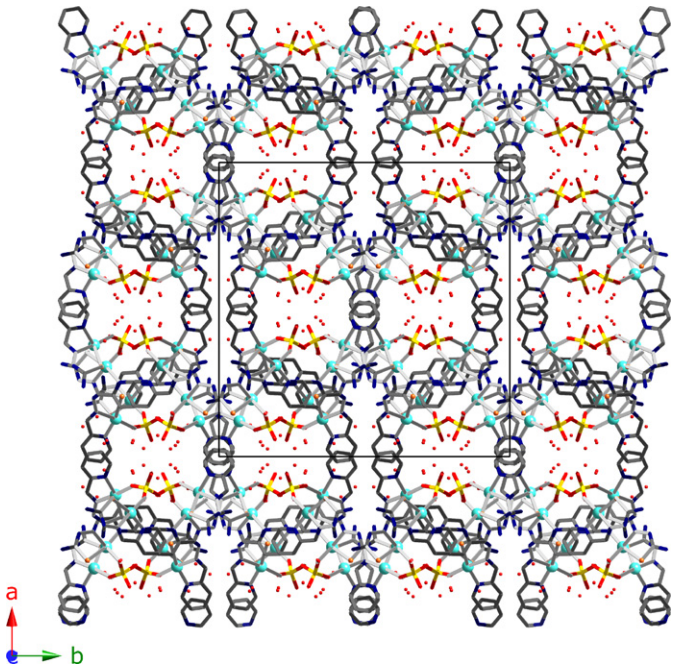

Fig. 28. A view of the crystal packing of compound **29**, showing the lattice water molecules residing into the channels created by the stacking of the tetranuclear unit along the crystallographic *c*-axis.

interactions, produces the honeycomb motif, which is illustrated in Fig. 28.

A second copper(II) tetranuclear complex has been isolated and characterized by Xu et al., of formula $\{[(hdpa)Cu(H_2O)(P_2O_7)Cu(hdpa)]_2\}\cdot 9H_2O$ **30** [15]. Compound **30** appears to be very similar to the previously reported zinc(II)-based compound of formula $\{[(bipy)Zn(H_2O)(\mu\text{-}P_2O_7)Zn(bipy)]_2\}\cdot 14H_2O$ **31** [73].

As shown in Fig. 29, **30** and **31** exhibit the same, centrosymmetric molecular arrangement, with the tetranuclear unit ideally built from the fusion of two distinct dimers upon removal of two apical (water) ligands.

The coordination environment about the two crystallographic independent copper(II) ions within the asymmetric unit of **30** is remarkably distorted, mainly due to the flexibility of the 2,2′-dipyridylamine ligand, but still closer to a square pyramid than a trigonal bipyramid (the trigonality parameter associated to the two ions is actually very different, being 0.068 for Cu1 and 0.45 for Cu2). The corresponding values in the asymmetric unit of **31** are instead much more similar and produce an average value of 0.61 (trigonal bipyramidal geometry for both Zn1 and Zn2 atoms).

The most relevant feature in compounds **30** and **31** is the innovative coordination mode adopted by the PPi anion. A quite similar coordination pathway has been already detected only in the dimeric triammonia–chromium pyrophosphato complex **16** [61]. However, in that case is the external, not equatorially coordinated oxygen atom to be involved in the axial bond, which in turn means that every pyrophosphate oxygen atom in **16** is still monodentate. Instead, in the case of **30** and **31**, one of the primarily bound oxygen atoms is bridging bismonodentate (μ_2) (compare Figs. 16 and 29). The asymmetric di-μ-O_{pyr} bridge deriving from the increased denticity of the anion in **30**–**31** contribute to separate the two symmetry-related Cu2 (**30**) and Zn1 (**31**) of a distance of ~3.24 and 3.12 Å, respectively [with the separation across the classic bis-bidentate pyrophosphate being ~4.94 in **30** and 5.16 Å in **31**].

The strong structural analogies between the tetrameric unit of these two compounds also translate in a very similar crystal packing to finally ended up with only small variations in the unit cell parameters (see crystallographic details in Table 10).

The interaction of the aromatic ligands through face-to-face intra- and intermolecular π–π stacking in **31** produces pseudo-layers parallel to the *bc*-plane, similarly to what already found in the other bipy- or phen-complexes discussed so far. A similar type of interaction can be also detected in **30** (although the dipyridylamine ligand as a whole can deviate sensibly from planarity), which lead to the formation of 2D sheets parallel to the [1–10] direction. The extensive presence of water molecules of crystallization ensures the cohesion of these sheets in the third dimension. An intricate network of hydrogen bonds can be found in both structures, as exemplified in Fig. 29d.

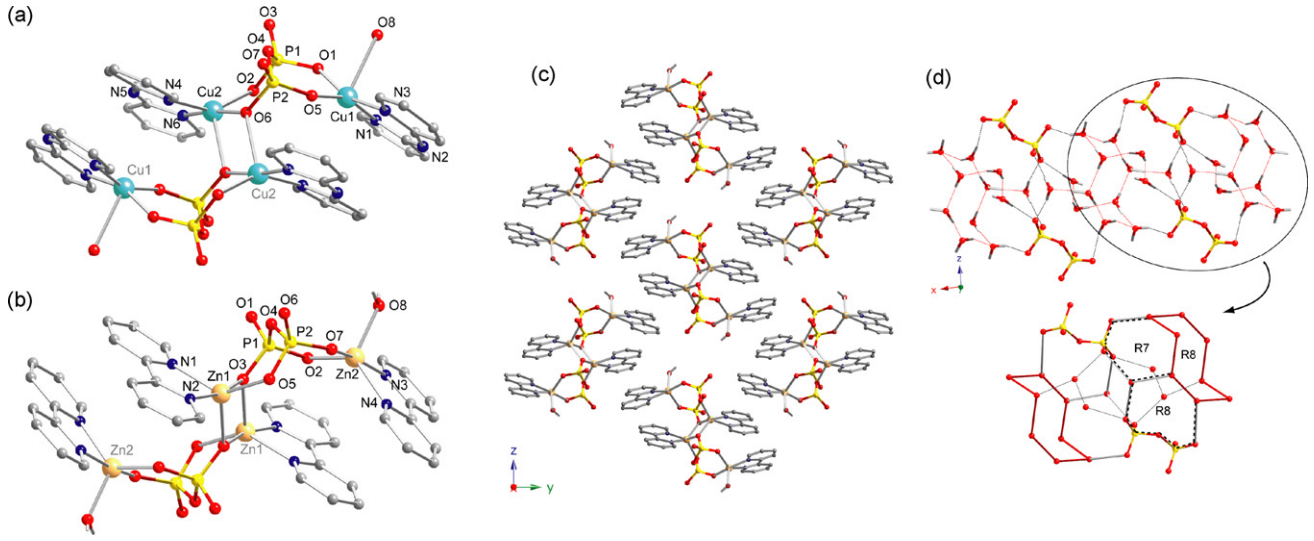

Fig. 29. (a) Crystal structure of the tetranuclear $\{[(dpa)Cu(H_2O)(P_2O_7)Cu(dpa)]_2\}$ unit in **30**, with the original labelling scheme and (b) crystal structure of the tetranuclear $\{[(bipy)Zn(H_2O)(\mu\text{-}P_2O_7)Zn(bipy)]_2\}$unit in **31**, with the original labelling scheme (hydrogen atoms on the dpa and bipy ligands not shown). (c) Crystal packing of **31** along the *a*-axis; (d) a view of the extensive network of hydrogen bonds involving the lattice water molecules and the pyrophosphate anions in **31**. Note that the intricate network can be viewed as sum of simpler water clusters or extended water-pyrophosphate motifs, as exemplified below, with the highlighted eight-membered water cluster (R8) and seven and eight-membered extended motifs R7 and R8) [79].

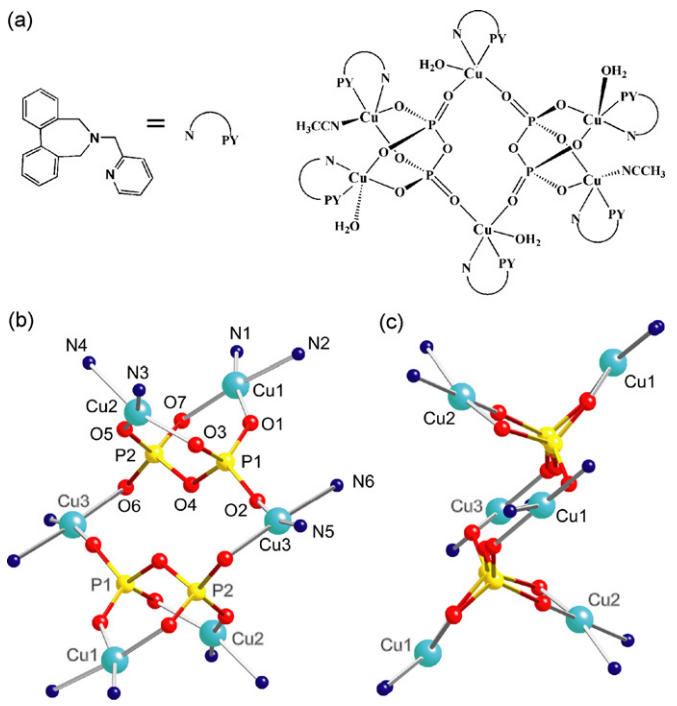

Fig. 30. (a) Schematic representation of the hexanuclear complex **32**; (b) and (c): two different side views of the hexa-copper(II) core of compound **32**, highlighting the metal–pyrophosphate coordination geometry [only the copper(II)-equatorial coordination environment is showed for clarity]. Within the complex, the metal–metal distances between adjacent copper ions range from 4.3 to 6.16 Å, while the diagonal ones fluctuate from 7.06 to 9.67 Å.

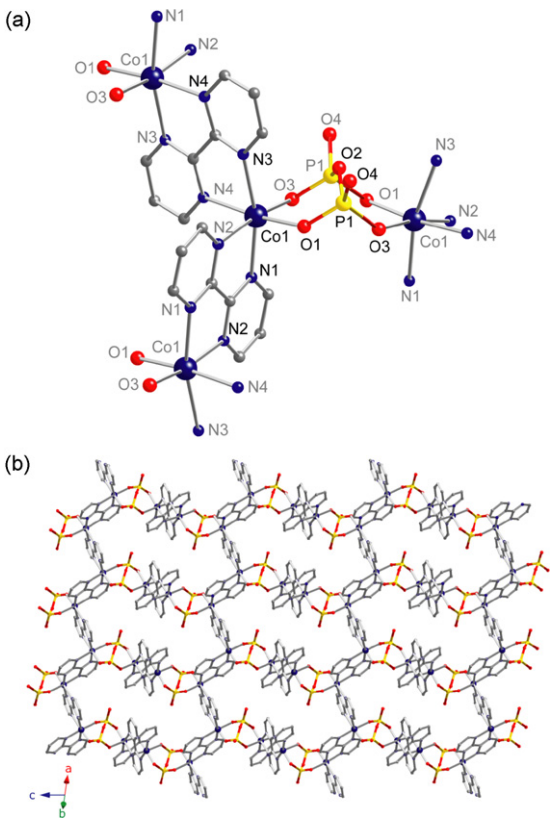

Fig. 31. (a) Molecular unit of the three-dimensional cobalt(II) compound **33** with the original labelling scheme; (b) a view of the crystal packing of **33** along the [1 1 − 1] direction.

2.4. Hexamers

2.4.1. Copper(II)

The hydrolysis reaction of a phosphodiester promoted by a di-μ-hydroxodicopper(II) complex has led, very recently, to the zero-dimensional pyrophosphate complex with the highest nuclearity known to date, the hexameric compound of formula $[(NPY)_6Cu_6(CH_3CN)_2(H_2O)_4(P_2O_7)_2](ClO_4)_4$ (**32**) [with NPY being an appositely built *N*,*N*-biphenyl-pyridine-appended ligand, see scheme in Fig. 4] [80].

The centrosymmetric hexacopper(II) unit can be viewed as the fusion of two classical bis-bidentate pyrophosphate-bridged dicopper(II) units linked by an additional O–Cu–O bridge (Fig. 30). Each copper(II) ion in **32** is five-coordinated, in a square pyramidal geometry, in which the basal positions are occupied by two nitrogen atoms from the NPY capping ligand and two oxygen atoms from a pyrophosphate group [with Cu3 being mono-coordinated to both the two different PPi ligands]. The apical position is filled by an acetonitrile [at Cu1] or a water molecule [at Cu2 and Cu3].

Of note, the pyrophosphate coordination mode in this complex resides exactly in between the more common bis-bidentate and octadentate ones, the latter being observed in the solid-state structure of the VPP catalyst [45,46].

2.5. Polymers

2.5.1. Cobalt(II)

The compound of formula $[Co_2(\mu\text{-}P_2O_7)(bpym)_2]\cdot 12H_2O$ (**32**) represents an unique example of high-dimensional pyrophosphate-bridged complex [16]. Previously discussed dimeric and tetrameric complexes featured nitrogen capping ligands such a 2,2′-bipyridine, 1,10′-phenanthroline. The three dimensionality of **32** was achieved by the incorporation of the bis-bidentate 2,2′-bipyrimidine ligand which in turn provides an alternate bridge in addition to the pyrophosphate one.

The divalent cobalt ion is in a distorted octahedral environment, being its coordination sphere occupied by four nitrogen atoms from two *cis* crystallographically unique bpym ligands and two oxygen atoms from the pyrophosphate tetraanion (see Fig. 31a). The Co–N [mean value of 2.164(1) Å] and Co–O_{pyr} [mean value of 2.035(1) Å] bond lengths are in agreement with literature data.

The pyrophosphato and bpym bridges produce a Co···Co separation of ∼5.30(1) and 5.81(1) Å. The overall metal ion connectivity results in the formation of large helical channels running along the [1 1 0] as well as the [1–10] directions (see Fig. 31b), which represent a solvent accessible void of ∼39% of the unit cell volume. Disordered lattice water molecules are confined in these channels and contribute to the three-dimensional stability, being involved in hydrogen bonding interactions with the anion oxygen atoms.

3. Magnetic interactions across the pyrophosphate bridge

Ainscough et al. were the first to synthesize a tetranuclear pyrophosphate-bridged coordination complex, the compound $[(CuL_3)_4(P_2O_7)]\cdot nH_2O$ (**29**), and to check the ability of pyrophosphate to mediate magnetic interactions between the paramagnetic metal centres [14].

The system was found to be weakly antiferromagnetic with a magnetic coupling value of $-3.7\ cm^{-1}$ (J is magnetic coupling with the Hamiltonian defined as $H = -JS_1S_2$). This weak antiferromagnetic coupling was determined to be a result of poor overlap of the magnetic orbitals (the molecular orbital which describes each unpaired electron is called magnetic orbital) through the three possible exchange pathways: (i) Cu–O–P–O–Cu (between Cu1–Cu4 and Cu2–Cu3), (ii) Cu–S–Cu [asymmetric bridge, with a long (axial)

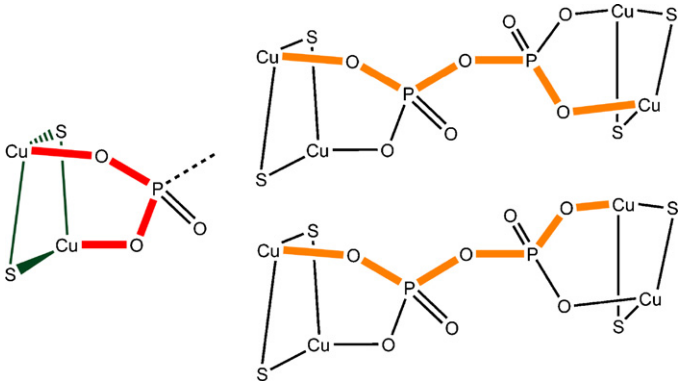

Fig. 32. Magnetic pathways involved in **29** [14].

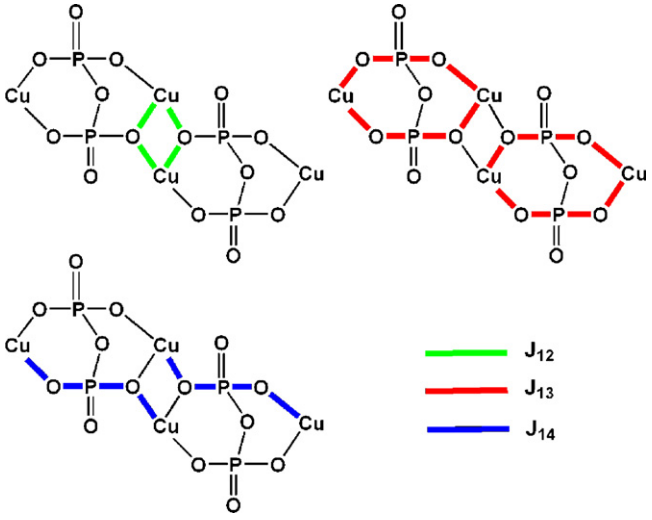

Fig. 33. Magnetic pathways observed in **30** [15].

and a short (equatorial) distance between Cu1–Cu4 and Cu2–Cu3], and (iii) Cu–O–P–O–P–O–Cu [between Cu1–Cu2 (or Cu3–Cu4) and Cu1–Cu3 (or Cu2–Cu4)] (see Fig. 32). The parallel arrangement of the involved magnetic orbitals in (i) and (ii) would lead to a very poor overlap and then to very weak magnetic interactions. The extended O–P–O–P–O path is the only one to be 'in plane' with the copper's magnetic orbitals and it is expected to be a poor mediator of magnetic interactions because its great length.

The work of Ainsough et al. has prompted the investigation of the magnetic interaction between paramagnetic metal ions through the pyrophosphate bridge and so, another tetranuclear compound of formula $\{[(hdpa)Cu(H_2O)(\mu\text{-}P_2O_7)Cu(hdpa)]_2\}\cdot 9H_2O$ (**30**) [15] was investigated too. An overall antiferromagnetic behavior was observed for **30**. There are three magnetic pathways observed in this complex: (i) the Cu–O–Cu bridge between the dimeric units, (ii) the *trans* and (iii) *cis* Cu–O–P–O–Cu across the pyrophosphate bridge (Fig. 33).

Of the three magnetic pathways, one contributes ferromagnetically ($J_{12} = +19\ cm^{-1}$) and the other two antiferromagnetically ($J_{13} = -46\ cm^{-1}$ and $J_{14} = -23\ cm^{-1}$), the strongest magnetic coupling being mediated by the bis-bidentate pyrophosphate bridge. The accidental orthogonality between the magnetic orbitals through the out-of-plane exchange pathway involving the double oxo-pyrophosphate bridge (i) would account for the ferromagnetic coupling. *Note*: The long M-O_t-P-O_b-P-O_t-M pathway has not been substantiated by magnetic study and magnetic complexes having only this pathway will be needed to achieve this.

In the structure of the dimeric pyrophosphate-bridged copper(II) complexes, $\{[Cu(bipy)(H_2O)]_2(\mu\text{-}P_2O_7)\}\cdot 7H_2O$ (**21**) [12] the coordinated water molecules are involved in hydrogen bonding (O–H···O) enabling intra- and intermolecular interactions. The intramolecular O–H···O bonding allows for an alternate magnetic pathway, in addition to the Cu–O–P–O–Cu route *via* the pyrophosphate bridge; with the latter providing the strongest path of communication. **21** was found to be weakly antiferromagnetic with a J value of $-20\ cm^{-1}$ ($H = -J\Sigma_i(S_{i-1}\cdot S_i - \alpha S_i\cdot S_{i+1})$ (α being the alternating parameter and S_i the local spin) [12].

The magnetic properties of **21** were also investigated as a function of degree of hydration in order to check the role of the hydrogen-bonding network on the magnetic behavior. Upon complete dehydration, the magnetic coupling became strongly antiferromagnetic with a coupling value of $-110\ cm^{-1}$, an increase of ca. five-fold (Fig. 34). This increase of the antiferromagnetic coupling in the anhydrous phase may be attributed to the formation of a Cu–$O_{(pyrophosphate)}$–Cu bridge between dimeric units through the loss of the water molecules [12].

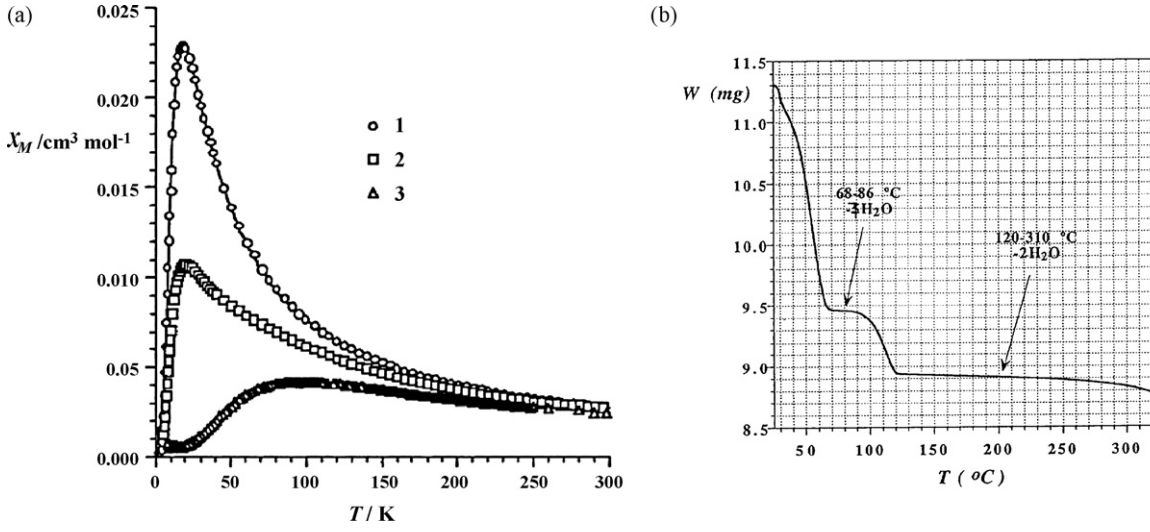

Fig. 34. (*Left*) Magnetic susceptibility of **21** as a function of degree of hydration. **1** is $\{[Cu(bipy)(H_2O)]_2(\mu\text{-}P_2O_7)\}\cdot 7H_2O$; **2** is $\{[Cu(bipy)(H_2O)]_2(\mu\text{-}P_2O_7)\}$ and **3** is $\{[Cu(bipy)]_2(\mu\text{-}P_2O_7)\}$. The loss of water is followed by TGA as shown (right). Images used with permission of the American chemical society and taken from reference [12].

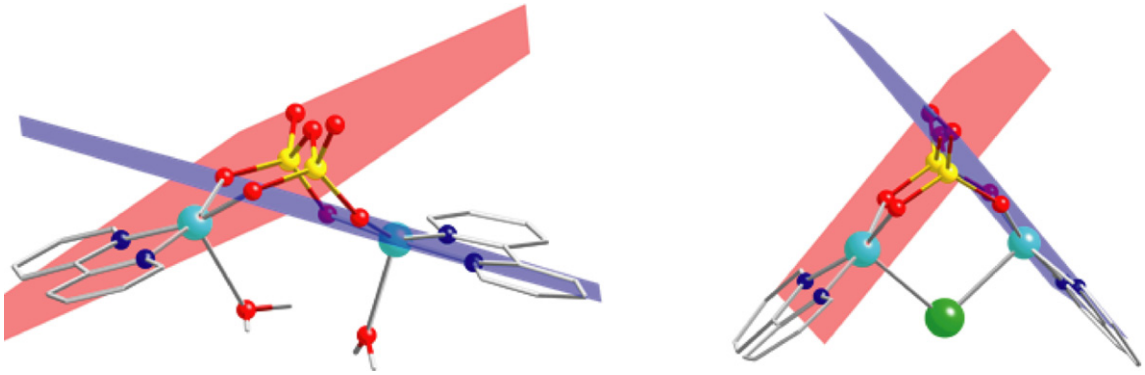

Fig. 35. Structure of **21** and **23** emphasizing the dihedral angle. Note the more acute angle of the dihedral angle between the basal plane of the copper atoms due to the incorporation of the additional chloro bridge.

The incorporation of an additional bridge can significantly affect the magnitude of the magnetic interaction across the pyrophosphate bridge, as exemplified by the {[Cu(bipy)]$_2$(μ-HP_2O_7)(μ-Cl)}·H_2O (**23**) [13]. The structure of this compound contains two copper(II) metal ions, capped by a 2,2′-bipyridine ligand in the basal plane. The pyrophosphate ligand is monoprotonated as a result of the incorporation of the chloro ion in the axial position. The magnetic coupling in **23** was found to be $-3.19\,cm^{-1}$ compared to $-20\,cm^{-1}$ for **21** [12,13]. The difference in the magnitude of the antiferromagnetic coupling is a result of the inclusion of the single chloro bridge. In this complex, the chloro ligand occupies the apical position of each copper(II)ion, thus the magnetic interaction across the Cu–Cl–Cu pathway is negligible as the magnetic orbitals ($d_{x^2-y^2}$) of the paramagnetic copper(II) ions reside in the equatorial plane. This additional bridge cause the dihedral angle between the basal plane of copper(II) ion to become more acute (see Fig. 35), a value of ∼133° in **21** *vs.* ∼84° in **23**. This subsequently causes an increase of the orthogonality across the Cu–O–P–O–Cu pathway. In so doing, the antiferromagnetic interaction across the bridge is decreased.

Once the ability of the pyrophosphate ligand to mediate magnetic interactions between copper(II) ions was established, divalent transition metal ions other than copper(II) were investigated in order to check the influence of the number of unpaired electrons on the magnetic coupling across the pyrophosphate bridge. The series of the dimanganese(II), dicobalt(II) and dinickel(II) compounds (**18**, **19** and **20**, respectively) are structural similar being comprised of neutral {[M^{II}(phen)$_2$]$_2$(μ-P_2O_7)} units with crystallographically unique metal(II) ions. The dinuclear entity consists of two [M^{II}(phen)$_2$]$^{2+}$ units which are bridged by the tetraanionic pyrophosphate ligand (see Fig. 18). The metal centres have a distorted octahedral geometry which is built by four nitrogen atoms from two phenanthroline ligands and two oxygen atoms from a pyrophosphate, providing each metal atom with an N_4O_2 donor set. In addition to their structural similarities, **18**, **29**, and **20** have been shown to exhibit weak intradimer antiferromagnetic couplings (see Table 11).

Most recently an exciting new result was obtained for the cobalt(II) compound [Co_2(μ-P_2O_7)(μ-bpym)$_2$]·$12H_2O$ (**32**) [16]. This 3D structure is the first pyrophosphate coordination complex to show a spin-canted antiferromagnetic behavior and it can be viewed as a significant step toward the preparation of high-T_c compounds (see Fig. 36). The compound behaves as a soft magnet with T_c ca. 19 K and a canting angle of ∼1.8° [16].

3.1. Magneto-structural correlations

The main advantage of pyrophosphate in respect to phosphate from a coordination chemistry viewpoint is the potential bidentate and bis-bidentate coordination modes of the former [96]. This feature provides a greater stability to the soluble pyrophosphate-containing complexes and also provides new exchange pathways to mediate electronic interactions between the bridged metal centres. The phosphate–pyrophosphate pair can be viewed as analogous to the acetate–oxalate couple. The magneto-structural studies of the acetate–oxalate pathways has been of upmost importance for over 50 years in the development of magneto-structural correlations. Research into pyrophosphate-bridged magnetic complexes, is still in its infancy and answers will be derived only from further magneto-structural investigations (the frontier between the ferro- and antiferromagnetic couplings, for instance).

The pyrophosphate ligand has been shown to mediate significant magnetic interactions between paramagnetic metal centres. In analyzing the magneto-structural properties of similar dimeric complexes, **18**–**22**, we focus on the exchange pathway provided by the two M(II)–O–P–O–M(II) arms. The poor overlap between these

Table 11
Magneto-structural data for pyrophosphate bridged complexes with divalent first-row transition metal ions.

Compound	M–O/Å[a]	d_{M-M}/Å[b]	d.a./°[c]	m.s.f.p./Å[d]	$-J/cm^{-1}$[e]	$-n_A{}^2J/cm^{-1}$[f]	References
Dimers							
{[Mn(phen)$_2$]$_2$(μ-P_2O_7)}·$13H_2O$ (**18**)	2.105(3)	4.700(1)	88.1	0.013, 0.001	0.88	22.0	[10]
{[Co(phen)$_2$]$_2$(μ-P_2O_7)}·6MeOH (**19**)	2.043(1)	4.857(1)	108.2	0.004, 0.019	1.23	11.1	[11]
{[Ni(phen)$_2$]$_2$(μ-P_2O_7)}·$27H_2O$ (**20**)	2.058(9)	5.031(2)	111.9	0.014, 0.102	3.8	15.2	[10]
{[Cu(bipy)(H_2O)]$_2$(μ-P_2O_7)}·$7H_2O$ (**21**)	1.951(4)	4.647(1)	132.2	0.226, 0.190	20	20	[12]
{[Cu(bipy)]$_2$(μ-HP_2O_7)(μ-Cl)}·H_2O (**23**)	1.950	3.954(1)	83.7	0.234, 0.185	3.19	3.19	[13]
Tetramers							
{[(hdpa)Cu(H_2O)(μ-P_2O_7)Cu(hdpa)]$_2$}·$9H_2O$ (**30**)	1.932	4.939	148	0.235, 0.035	50.2[g]	50.2[g]	[15]

[a]Average value for the metal–oxygen (bridging pyrophosphato ligand) bond distances, [b]metal–metal separation across the pyrophosphato ligand, [c]*for Cu(II) complexes:* Dihedral angle between the mean basal planes of the two metal ions in the dimeric unit. *For all other complexes:* Dihedral angle between the [N_2O_2] planes of the two metal ions in the dimeric unit (*see text*), [d]metal shift from the plane defined in *c*; the two given values correspond to the two independent atoms in the dimeric unit, [e]*J* is the magnetic coupling through the bridging pyrophosphato. [f]n_A is the number of the unpaired electrons on the metal atom A of the homodinuclear AA complex. [g]This value corresponds to the magnetic coupling through the bis-bidentate pyrophosphate (as for the other examples in this table).

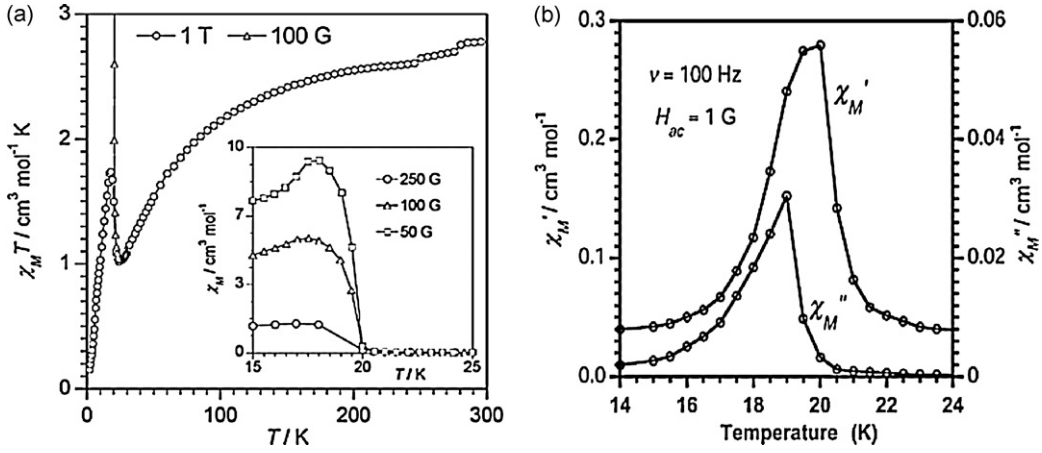

Fig. 36. (a) Thermal variation of **32**. Inset shows χ_M *vs.* *T* at different values of dc magnetic field. (b) In- and out-of-phase ac susceptibility *vs.* *T* for **32** in the lack of a dc magnetic field. Images used with permission of the Royal Society of Chemistry and are taken from reference [16].

two magnetic orbitals through the two nonlinear O–P–O bridging motifs accounts for the weak antiferromagnetic coupling. The number of unpaired electrons increases along this series from one in Cu^{II} to five in Mn^{II}, with additional σ- and π-pathways becoming operative. The magnitude of the antiferromagnetic interaction for such a series is best described not by *J*, but by $n_A n_B J$ (see Table 11). As the energy of the 3d orbitals decreases when going from Mn^{II} to Cu^{II}, the energy gap between these orbitals and that of the symmetry-adapted HOMOs of the bridging pyrophosphate ligand becomes smaller. The decreasing energy gap from Mn^{II} to Cu^{II} would result in better overlap between the magnetic orbitals from Mn^{II} to Cu^{II} and cause an increase in the magnitude of the antiferromagnetic interaction along these series. This general trend is observed for the Co^{II}, Ni^{II} and Cu^{II} pyrophosphate complexes, but the antiferromagnetic coupling in the case of the Mn^{II} is too large. Most likely, the origin of this discrepancy lies on subtle structural differences. In fact, the intramolecular metal–metal separation in the manganese compound is nearly equal to that of the copper(II) compound and significantly smaller than those of the corresponding cobalt(II) and nickel(II) complexes. The greater distortion of the manganese N_4O_2 chromophore could cause a strengthening of the overlap between the interacting magnetic orbitals and thus a greater antiferromagnetic coupling.

A structural parameter of particular relevance for these pyrophosphate-bridged complexes concerns the dihedral angle between the two basal/equatorial mean planes within the dinuclear unit. The dihedral angle increases going from manganese(II) to copper(II), with exception of the pyrophosphate-chloride-bridged complex **23**. A comparison between the two dicopper(II) complexes (**21** and **23**) clearly shows that the value of the antiferromagnetic coupling decreases as the dihedral angle is decreased ($J = -20\ cm^{-1}$ in **21** *vs.* $-3.2\ cm^{-1}$ in **23**, the values of dihedral angles being 132.2° and 83.7°, respectively). The more acute dihedral angle enables increased orthogonality through the M–O–P–O–M pathway, effectively minimizing the antiferromagnetic interaction across the pyrophosphate bridge.

4. Biological properties of pyrophosphate complexes

Despite the biological significance of pyrophosphate and the growing library of pyrophosphate coordination complexes, the antiproliferative properties of these complexes have yet to be explored extensively. Bose et al. [17] and Doyle and co-workers [18] have investigated the cytotoxicity of monomeric platinum(II/IV) and dimeric nickel(II), copper(II), and cobalt(II) pyrophosphate complexes.

Bose et al. published mononuclear Pt(II) and Pt(IV) pyrophosphate complexes exhibiting micromolar cytotoxic activity against cisplatin resistant cancer cells [17]. Five compounds were investigated (see Fig. 37) but crystal structures were obtained for only two of such compounds (compounds **14** and **15** discussed above).

The cytotoxicity of these compounds was tested in human ovarian cancer cells A2780 and in the cisplatin/carboplatin cross-resistant cell line A2780/C30. The IC_{50} values are shown in Table 12. Of all the mononuclear platinum–pyrophosphate compounds tested, dach-2 exhibited the highest toxicity, 20 μM in the parent cell line and 48 μM in the cross-resistant cells. Unlike cisplatin, dach-2 does not bind to DNA, instead its toxicity is the result of enzyme inhibition [17].

Doyle et al. have investigated the cytotoxicity of three pyrophosphate-bridged complexes (**19**–**21**) with varying metal centres (cobalt, copper, and nickel) [18]. As previously discussed, these complexes are structurally analogous with a $\{[M^{II}(phen)_2]_2(\mu\text{-}P_2O_7)\}$ core (see Fig. 25). The compounds were tested in adriamycin-resistant human ovarian cancer cell line (A2780/AD) over varying time points, 24 and 72 h shown in Table 13.

Significant toxicities were observed in **19** and **21**; exhibiting low nanomolar [1.77 nM] and picomolar [169 pM] IC_{50} values respec-

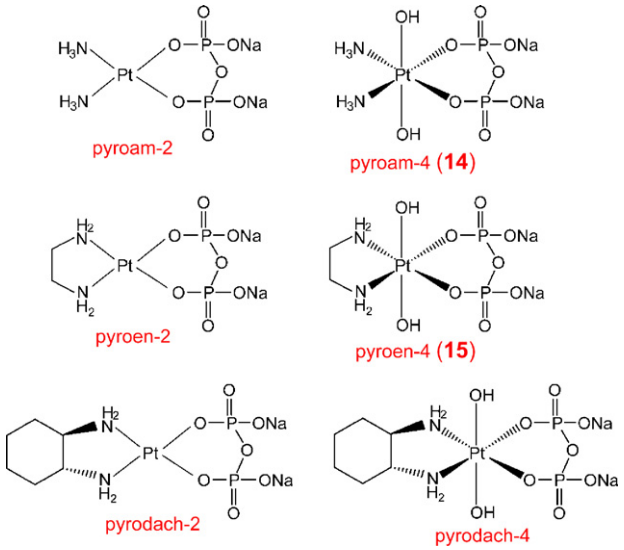

Fig. 37. Structure of mononuclear platinum–pyrophosphate complexes.

Table 12
IC_{50} values [μM] of mononuclear pyrophosphate-containing Pt(II) and Pt(IV) compounds, cisplatin, and carboplatin in A2780, A2780/C30 and Chinese Hamster Ovary (CHO) ovarian cells.

Compound		A2780	A2780/C30	CHO
Cisplatin		70 ± 1	100 ± 11	29 ± 3
Carboplatin		90 ± 13	>200	>200
(*trans*-1,2-Cyclohexanediamine)(dihydrogenpyrophosphato)platinum(II)	**pyrodach-2**	20 ± 4	48 ± 5	35 ± 5
(*trans*-1,2-Cyclohexanediamine)-*trans*-dihydroxo (dihydrogenpyrophosphato)platinum(IV)	**pyrodach-4**	180 ± 15	155 ± 17	116 ± 17
Diammine(dihydrogenpyrophosphato)platinum (II)	**pyroam-2**	100 ± 11	>200	120 ±30
cis-Disammine-*trans*-dihydroxo(dihydrogenpyrophosphato)platinum(IV)	**14**	175 ± 22	>200	>200
1,2-Ethanediamine-*trans*-dihydroxo(dihydrogenpyrophosphato)platinum(II)	**15**	170 ± 33	>200	>200

Table 13
IC_{50} value [μM] of pyrophosphate bridged homodinuclear nickel(II), copper(II) and cobalt(II) complexes compared with cisplatin, in A2780 and A2780AD cell lines.

Complex		IC_{50} [μM]	
		24 h	72 h
$\{[Ni(phen)_2]_2(\mu\text{-}P_2O_7)\}\cdot 27H_2O$	**20**	589.1 ± 31.6	304.0 ± 40.9
$\{[Cu(phen)(H_2O)]_2(\mu\text{-}P_2O_7)\}\cdot 8H_2O$	**21**	0.64 ± 0.12	$(1.77 \pm 0.15) \times 10^{-3}$
$\{[Co(phen)_2]_2(\mu\text{-}P_2O_7)\}\cdot 6MeOH$	**19**	2.01 ± 0.86	$(1.69 \pm 0.54) \times 10^{-4}$
cis-$[Pt(NH_3)_2Cl_2]$		84.0 ± 10.3	11.0 ± 1.5

tively at 72 h. These systems have been shown to be activated *via* the hydrolysis of the pyrophosphate ligand, enabling cellular entry. The extreme toxicity of these complexes can be attributed to the ability of such compounds to inhibit enzymes, particularly topoisomerase I, interact with DNA, and induce oxidative stress [18].

5. Conclusion and outlook

Pyrophosphate as a ligand has already made a huge impact in catalysis and is now expanding into structural, functional and biological arenas. Pyrophosphate coordination complexes have properties ranging from picomolar cytotoxicity, to the industrial conversion of butane to maleic anhydride, to spin canted magnetic phenomena and multidimensional structures. Considering the diversity of structures and associated functions noted to date, this despite the relative paucity of examples, it is clear only the surface of pyrophosphate coordination chemistry has been scratched. To date, in fact, no luminescent, ferromagnetic, catalytic or even lanthanide coordination complex has been reported. There is then an extraordinary amount of "untapped" potential in using the pyrophosphate anion to produce complexes with a variety of structural motifs and magnetic exchange pathways and to use pyrophosphate in drugs and/or pro-drugs. We look forward to pursuing these areas in the future.

Acknowledgments

R.P.D. wishes to acknowledge the American Chemical Society for a Doctoral New Investigator Award (48999-DNI 3). M.J. thanks the Spanish Ministry of Ciencia e Innovación and the Generalitat Valenciana for the funds through the projects Consolider Ingenio CSD-2007-00010 (Molecular Nanoscience) and Prometeo/2009/198, respectively.

Appendix A. Supplementary data

Supplementary data associated with this article can be found, in the online version, at doi:10.1016/j.ccr.2009.12.015.

References

[1] J.E. Walker, Angew. Chem. 110 (1998) 2438;
J.E. Walker, Angew. Chem. Int. Ed. 37 (1998) 2308.
[2] P.D. Boyer, Angew. Chem. 110 (1998) 2424;
P.D. Boyer, Angew. Chem. Int. Ed. 37 (1998) 2296.
[3] L. Ernester, Molecular Mechanism in Bioenergetics, Elsevier, Amsterdam, 1992.
[4] W.N. Lipscomb, N. Strater, Chem. Rev. 96 (1996) 2375.
[5] I.S. Kulaev, V.M. Vagabov, T.V. Kulakovskaya, The Biochemistry of Inorganic Polyphosphates, 2nd ed., John Wiley & Sons, Ltd., Chichester, 2004.
[6] R.L.P. Adams, J.T. Knowler, D.P. Leader, The Biochemistry of Nucleic Acids, 10th ed., Chapman and Hall, London, 1986.
[7] G. Centi, F. Trifiro, J.R. Ebner, V. Franchetti, Chem. Rev. 88 (1988) 55 (and references therein).
[8] B. Chen, E.J. Munson, J. Am. Chem. Soc. 124 (2002) 1638 (and references therein).
[9] N. Ballarini, F. Cavani, C. Cortelli, S. Ligi, F. Pierelli, F. Trifiro, C. Fumagalli, G. Mazzoni, T. Monti, Top. Catal. 38 (2006) 147 (and references therein).
[10] O.F. Ikotun, N.G. Armatus, M. Julve, P.E. Kruger, F. Lloret, M. Nieuwenhuyzen, R.P. Doyle, Inorg. Chem. 46 (2007) 6668.
[11] O.F. Ikotun, W. Ouellette, F. Lloret, P.E. Kruger, M. Julve, R.P. Doyle, Eur. J. Inorg. Chem. 17 (2008) 2691.
[12] P.E. Kruger, R.P. Doyle, M. Julve, F. Lloret, M. Nieuwenhuyzen, Inorg. Chem. 40 (2001) 1726.
[13] O.F. Ikotun, E.M. Higbee, W. Ouellette, F. Lloret, M. Julve, R.P. Doyle, Eur. J. Inorg. Chem. 33 (2008) 5281.
[14] E.W. Ainscough, A.M. Brodie, J.D. Ranford, J.M. Waters, K.S. Murray, Inorg. Chim. Acta 197 (1992) 107.
[15] J.-Y. Xu, J.-L. Tian, Q.-W. Zhang, J. Zhang, S.-P. Yan, D.-Z. Liao, Inorg. Chem. Commun. 11 (2008) 69.
[16] N. Marino, T.F. Mastropietro, D. Armentano, G. De Munno, R.P. Doyle, F. Lloret, M. Julve, Dalton Trans. 38 (2008) 5152.
[17] (a) R.N. Bose, L. Maurmann, R.J. Mishur, L. Yasui, S. Gupta, W.S. Grayburn, H. Hofstetter, T. Salley, PNAS (USA) 105 (2008) 18314;
(b) R.J. Mishur, C. Zheng, T.M. Gilbert, R.N. Bose, Inorg. Chem. 47 (2008) 7972.
[18] O.F. Ikotun, E.M. Higbee, W. Ouellette, R.P. Doyle, J. Inorg. Biochem. 103 (2009) 1254.
[19] G.M. Blackburn, M.J. Gaits, Nucleic Acids in Chemistry and Biochemistry, 2nd ed., Oxford University Press, New York, 1996.
[20] J.M. Berg, J.L. Tymoczko, L. Stryer, Biochemistry, 5th ed., W.H. Freedman & Co., New York, 2002.
[21] K.M. Welsh, I.M. Armitage, B.S. Cooperman, Biochemistry 22 (1983) 1046.
[22] P. Heikinheimo, P. Pohjanjoki, A. Helminen, M. Tasanen, B.S. Cooperman, A. Goldman, A. Baykov, R. Lahti, Eur. J. Biochem. 239 (1996) 138.
[23] A.A. Baykov, B.S. Cooperman, A. Goldman, R. Lahti, Prog. Mol. Subcell Biol. 23 (1999) 127.
[24] H.D. Kay, Biochem. J. 22 (1928) 1446.
[25] M. Maeshima, Eur. J. Biochem. 196 (1991) 11.
[26] L.S. Motta, W.S. da Silva, D.M. Oliveira, W. de Souza, E.A. Machado, Insect Biochem. Mol. Biol. 34 (2004) 19.
[27] D.E. Wilcox, Chem. Rev. 96 (1996) 2435.
[28] D. Westfall, N. Aboushadi, J.E. Shackelford, S.K. Krisans, Biochem. Biophys. Res. Commun. 230 (1997) 562.
[29] D.A. Gdula, R. Sandaltzopoulos, T. Tsukiyama, V. Ossipow, C. Wu, Genes. Dev. 12 (1998) 3206.
[30] E.H. Harutyunyan, I.P. Kuranova, B.K. Vainshtein, W.E. Hohne, V.S. Lamzin, Z. Dauter, A.V. Teplyakov, K.S. Wilson, Eur. J. Biochem. 239 (1996) 220.
[31] M.R. Gomez-Garcia, M. Losada, A. Serrano, Biochem. J. 395 (2006) 211.
[32] M. Maeshima, Biochim. Biophys. Acta 1465 (2000) 37.
[33] R. Docampo, S.N. Moreno, Mol. Biochem. Parasitol. 114 (2001) 151.
[34] J.R. Perez-Castineira, J. Alvar, L.M. Ruiz-Perez, A. Serrano, Biochem. Biophys. Res. Commun. 294 (2002) 567.
[35] C.O. Rodrigues, D.A. Scott, B.N. Bailey, W. De Souza, M. Benchimol, B. Moreno, J.A. Urbina, E. Oldfield, S.N. Moreno, Biochem. J. 349 (2000) 737.
[36] E. Bordes, P. Courtine, J. Catal. 57 (1979) 236.
[37] G. Busca, G. Centi, F. Trifiro, Appl. Catal. 25 (1986) 265.
[38] (a) R.L. Bergman, N.W. Frisch, US Patent 3 293 268 (1966);
(b) S.H. Sookraj, D. Engelbrecht, Catal. Today 49 (1991) 161.
[39] C.C. Torardi, J.C. Calabrese, Inorg. Chem. 23 (1984) 1308.
[40] J.W. Johnson, D.C. Johnston, A.J. Jacobson, J.F. Brody, J. Am. Chem. Soc. 106 (1984) 8123.
[41] M.E. Leonowicz, J.W. Johnson, J.F. Brody, H.F. Shannon, J.M. Newsam, J. Solid State Chem. 56 (1985) 370.

[42] V.V. Guliants, S.A. Holmes, J.B. Benziger, P. Heaney, D. Yates, L.E. Wachs, J. Mol. Catal. A: Chem. 172 (2001) 265.
[43] Yu.E. Gorbunova, S.A. Linde, Sov. Phys. Dokl. 24 (1979) 138.
[44] P.T. Nguyen, R.D. Hoffman, A.W. Sleight, Mater. Res. Bull. 30 (1995) 1055.
[45] Z. Hiroi, M. Azuma, Y. Fujishiro, T. Saito, M. Takano, F. Izumi, T. Kamiyama, T. Ikeda, J. Solid State Chem. 146 (1999) 369.
[46] S. Geupel, K. Pilz, S. van Smaalen, F. Bullesfeld, A. Prokofiev, W. Assmus, Acta Crystallogr. C 58 (2002) i9.
[47] J.R. Ebner, M.R. Thompson, Structure-Activity and Selectivity Relationships in Heterogenoeous Catalysis, Elsevier, Amsterdam, 1991.
[48] E. Bordes, P. Courtine, J.W. Johnson, J. Solid State Chem. 55 (1984) 270.
[49] P. Amoros, R. Ibanez, A. Beltran, D. Beltran, A. Fuertes, P. Gomez-Romero, E. Hernandez, J. Rodriguez-Carvajal, Chem. Mater. 3 (1991) 407.
[50] C.C. Torardi, Z.G. Li, H.S. Horowitz, W. Liang, M.-H. Whangbo, J. Solid State Chem. 119 (1995) 349.
[51] H. Imai, Y. Kamiya, T. Okuhara, J. Catal. 255 (2008) 213.
[52] D.C. Johnston, J.W. Johnson, D.P. Goshorn, A.J. Jacobson, Phys. Rev. B 35 (1987) 219.
[53] E. Dagotto, J. Riera, D. Scalapino, Phys. Rev. B 45 (1992) 5744.
[54] E. Dagotto, T.M. Rice, Science 271 (1996) 618.
[55] N. Herron, D.I. Thorn, R.L. Harlow, G.W. Coulston, J. Am. Chem. Soc. 110 (1997) 7149.
[56] A. Muller-Hartmann, H. Vahrenkamp, Eur. J. Inorg. Chem. (2000) 2355.
[57] B.S. Cooperman, Metal Ions in Biochemistry, vol. 5, Marcel Dekker, New York, 1976.
[58] P. Chaudhuri, H. Sigel, J. Am. Chem. Soc. 99 (1977) 3142.
[59] T.R. Howard, J.B. Lee, R.H. Grubbs, J. Am. Chem. Soc. 102 (1980) 6878.
[60] T.P. Haromy, W.B. Knight, D. Dunaway-Mariano, M. Sundaralingam, Acta Cryst. C40 (1984) 223.
[61] T.P. Haromy, C.F. Linck, W.W. Cleland, M. Sundaralingam, Acta Cryst. C46 (1990) 951.
[62] T.P. Haromy, J. Rawlings, W.W. Cleland, M. Sundaralingam, Acta Cryst. C46 (1990) 2369.
[63] E.A. Merritt, M. Sundaralingam, D. Dunaway-Mariano, J. Am. Chem. Soc. 103 (1981) 3565.
[64] U. Kortz, Inorg. Chem. 39 (2000) 623.
[65] D. Cremer, J.A. Pople, J. Am. Chem. Soc. 97 (1975) 1354.
[66] S. Ahmed, A. Samah, R. Mohamed, Acta Crystallogr. Sect. E: Struct. Rep. Online 62 (2006) m1796.
[67] A. Selmi, S. Akriche, M. Rzaigui, Anal. Sci.: X-ray Struct. Anal. Online 22 (2006) x135.
[68] F. Capitelli, B. El Bali, R. Essehli, M. Lachkar, V. Valentini, G. Mattei, J. Taraba, Z. Zak, Z. Kristallogr. 221 (2006) 649.
[69] A. Gharbi, A. Jouini, J. Chem. Cryst. 34 (2004) 727.
[70] R. Essehli, B. El Bali, M. Lachkar, I. Svoboda, H. Fuess, Acta Crystallogr. Sect. E: Struct. Rep. Online 62 (2006) m538.
[71] L.M. Engelhardt, E.A. Keegan, G.A. Lawrance, A.H. White, Aust. J. Chem. 42 (1989) 1045.
[72] A. Gharbi, A. Jouini, M.T. Averbuch-Pouchot, A. Durif, J. Solid State Chem. 111 (1994) 330.
[73] R.P. Doyle, M. Nieuwenhuyzen, P.E. Kruger, Dalton Trans. (2005) 3745.
[74] A.W. Addison, T.N. Rao, J. Reedijk, J. Van Rijn, G.C. Verschoor, J. Chem. Soc. Dalton Trans. (1984) 1349.
[75] D. Armentano, G. De Munno, R. Rossi, New J. Chem. 30 (2006) 13 (and references therein).
[76] Y. Funahashi, A. Yoneda, C. Taki, M. Kosuge, T. Ozawa, K. Jitsukawa, H. Masuda, Chem. Lett. 34 (2005) 1332 (and references therein).
[77] D.H. Lee, J.H. Im, S.U. Son, Y.K. Chung, J.-I. Hong, J. Am. Chem. Soc. 125 (2003) 7752.
[78] J.H. Lee, J. Park, M.S. Lah, J. Chin, J.-I. Hong, Org. Lett. 9 (2007) 3729.
[79] (a) L. Infantes, S. Motherwell, Cryst. Eng. Commun. 4 (2002) 454;
(b) L. Infantes, J. Chisholm, S. Motherwell, Cryst. Eng. Commun. 5 (2003) 480;
(c) M. Mascal, L. Infantes, J. Chisholm, Angew. Chem. Int. Ed. 45 (2006) 32.
[80] S. Sabiah, B. Varghese, N.N. Murthy, Chem. Commun. (2009) 5636.
[81] X.-Y. Yi, Q.-F. Zhang, T.C.H. Lam, E.Y.Y. Chan, I.D. Williams, W.-H. Leung, Inorg. Chem. 45 (2006) 328.
[82] U. Kortz, G.B. Jameson, M.T. Pope, J. Am. Chem. Soc. 116 (1994) 2659.
[83] (a) S. Himeno, A. Saito, T. Hori, Bull. Chem. Soc. Jpn. 63 (1990) 1602;
(b) U. Kortz, M.T. Pope, Inorg. Chem. 33 (1994) 5643.
[84] U. Kortz, Inorg. Chem. 39 (2000) 625.
[85] C. du Peloux, P. Mialane, A. Dolbecq, J. Marrot, F. Sécheresse, Angew. Chem. 114 (2002) 2932;
C. du Peloux, P. Mialane, A. Dolbecq, J. Marrot, F. Sécheresse, Angew. Chem. Int. Ed. 41 (2002) 2808.
[86] Q. Li, S.-W. Zhang, Z. Anorg. Allg. Chem. 631 (2005) 2490.
[87] A.M. Chippindale, Chem. Mater. 12 (2000) 818.
[88] M.A. Salvado, P. Pertierra, C. Trobajo, J.R. Garcia, J. Solid State Chem. 181 (2008) 1103.
[89] Y. Liu, L. Zhang, Z. Shi, H. Yuan, W. Pang, J. Solid State Chem. 158 (2001) 68.
[90] J.L. Kissick, A.M. Chippindale, Acta Crystallogr. Sect. E: Struct. Rep. Online 58 (2002) m80.
[91] F. Millange, R.I. Walton, N. Guillou, T. Loiseau, D. O'Hare, G. Ferey, Chem. Mater. 14 (2002) 4448.
[92] F. Millange, R.I. Walton, N. Guillou, T. Loiseau, D. O'Hare, G. Ferey, Chem. Commun. (2002) 826.
[93] N. Stock, G. Ferey, A.K. Cheetham, Solid State Sci. 2 (2000) 307.
[94] F. Capitelli, B. El Bali, R. Essehli, M. Lachkar, I. da Silva, Z. Kristallogr. 221 (2006) 788.
[95] J.W. Johnson, D.C. Johnston, H.E. King Junior, T.R. Halbert, J.F. Brody, D.P. Goshorn, Inorg. Chem. 27 (1988) 1646.
[96] R.P. Doyle, T.H. Bauer, J. Cano, F. Lloret, M. Nieuwenhuyzen, M. Julve, Dalton Trans. 44 (2007) 5140.
[97] (a) T. Shintani, T. T.Uchiumi, T. Yonezawa, A. Salminen, A.A. Baykov, R. Lahti, A. Hachimori, FEBS Lett. 439 (1998) 263;
(b) N.J. Kuhn, A. Wadeson, S. Ward, T.W. Young, Arch. Biochem. Biophys. 379 (2000) 292.
[98] M.R. Gomez-Garcia, L.M. Ruiz-Perez, D. Gonzalez-Pacanowska, A. Serrano, FEBS Lett. 560 (2004) 158.
[99] M.R. Gómez-García, M. Losada, A. Serrano, FEBS J. 274 (2007) 3948.
[100] M. Perrotte-Piquemal, A. Danchin, F. Bivelle, Biochimie 81 (1999) 245.